

REPORT DOCUMENTATION PAGE			Form Approved OMB No. 0704-0188	
Public reporting burden for this collection of information is estimated to average 1 hour per response, including the time for reviewing instructions, searching existing data sources, gathering and maintaining the data needed, and completing and reviewing the collection of information. Send comments regarding this burden estimate or any other aspect of this collection of information, including suggestions for reducing this burden, to Washington Headquarters Services, Directorate for Information Operations and Reports, 1215 Jefferson Davis Highway, Suite 1204, Arlington, VA 22202-4302, and the Office of Management and Budget, Paperwork Reduction Project (0704-0188), Washington, DC 20503.				
1. AGENCY USE ONLY (Leave Blank)		2. REPORT DATE 29Mar99		3. REPORT TYPE AND DATES COVERED Final Report, 20Aug98 - 19Feb99
4. TITLE AND SUBTITLE High Density Optical Interconnection Based On Free Space Non-Diffracting Beams			5. FUNDING NUMBERS DASG60-98-M-0156	
6. AUTHOR(S) Michael R. Wang				
7. PERFORMING ORGANIZATION NAME (S) AND ADDRESS(ES) New Span Opto-Technology Inc. Sunset Office Park, A-142 9370 SW 72nd Street Miami, FL 33173			8. PERFORMING ORGANIZATION REPORT NUMBER NSOT 0201REP-BMDO	
9. SPONSORING/MONITORING AGENCY NAME(S) AND ADDRESS(ES) Sponsoring: BMDO, TOI/SBIR(BOND) 1725 Jefferson Davis Highway, Suite 809 Arlington, VA 22202 Monitoring: US Army Space and Missile Defense Command Huntsville, AL 35807			10. SPONSORING/MONITORING AGENCY REPORT NUMBER	
11. SUPPLEMENTARY NOTES The project is performed in collaboration with the Dept. of Electrical and Computer Engineering, University of Miami.				
12a. DISTRIBUTION/AVAILABILITY STATEMENT Unrestricted			12b. DISTRIBUTION CODE	
13. ABSTRACT (Maximum 200 words) Optical interconnects are required for high speed opto-electronic packaged computing systems for fast access to large intelligent database and for fast image data processing. However, existing free space optical interconnection suffers from diffraction limitation of interconnect line density and requires many large and sophisticated beam collimation, focusing, and interconnect reconfiguration elements. It is preferred to have small interconnection beams and with large interconnection distance. Such contradictory requirement is not possible by conventional Gaussian optical beams propagating in free space. It is however possible using non-diffracting beams since the diffraction contribution of the non-diffracting beam permits the beam to propagate in free space for a substantially large distance without significant beam size broadening. In this Phase I STTR program New Span Opto-Technology Inc. in collaboration with University of Miami demonstrated the feasibility of high-density optical interconnection based on free space non-diffracting beams. Using a diffractive beam shaper we achieved 87% efficiency. We also achieved 100 micron beam propagation of 40 cm range.				
14. SUBJECT TERMS Optical Interconnects, Diffractive, Non-Diffracting Beam, Beam Shaping			15. NUMBER OF PAGES 48	
			16. PRICE CODE	
17. SECURITY CLASSIFICATION OF REPORT UNCLASSIFIED	18. SECURITY CLASSIFICATION OF THIS PAGE UNCLASSIFIED	19. SECURITY CLASSIFICATION OF ABSTRACT UNCLASSIFIED	20. LIMITATION OF ABSTRACT UL	

REF D

Standard Form 298 (Rev. 2-89)  
Prescribed by ANSI Std. Z39-18  
298-102

DTIC QUALITY INSPECTION

## 1.0 INTRODUCTION

Optical interconnection is important for high-speed computing system. It offers several advantages, including the ability to achieve high data rate signal transmission, large fanout densities, and the ability to reduce capacitive and inductive loading effects<sup>[1-17]</sup>. Because of their high speed and wide bandwidth capabilities, with interconnect parameters independent of interconnection distance, optical interconnects are excellent candidates to replace electrical interconnects in a variety of applications, including those which require high-data-rate operation ( $> 1$  Gb/s), long distance signal propagation ( $>$  a few mm), low power consumption, and immunity to radiation and EMI<sup>[4]</sup>. A comparison between optical and electrical interconnects, based on power and speed considerations<sup>[4]</sup>, has shown that, at data speeds  $> 3$  GHz, the switching energy for electrical interconnects increases abruptly, making them unsuitable for practical systems. Crosstalk and EMI effects would further degrade their performance, thereby making optical interconnects very attractive for chip-to-chip and board-to-board applications. Optical interconnection is thus very useful for fast computing and image data processing for military applications such as missile interception, target identification, fast access to large intelligent database, and for commercial applications such as medical image data processing.

Recently, there is significant interest on board-to-board optical interconnects since the interconnection distance is long. For board-to-board interconnects, the existing interconnection architectures are:

- Free space optical interconnection
  - Free space board-to-board direct interconnection
  - Unconfined beam propagating in optical backplane substrate for board-to-board interconnection
- Guided-wave optical interconnection
  - Guided-wave optical backplane interconnection
  - Fiber or fiber ribbon for board-to-board interconnection

These interconnection architectures have their advantages and drawbacks. Free space interconnection is flexible and easier for interconnect pattern reconfiguration but the interconnect density is limited by the optical beam diffraction. In other words, the optical beam is preferred to be collimated to allow longer distance propagation without experiencing significant beam divergence. This requires relatively large collimation lenses and collection/focusing lenses. The interconnect density is set by the lens center to center distance. The collimating beam requirement can be released by using holographic multiple focusing elements but it suffers from the critical alignment requirement of the holographic optical elements. The optical backplane substrate interconnects use unconfined beams propagating under total-internal-reflection in a transparent optical substrate such as a glass. The performance is similar to free space interconnection and is thus limited by the optical beam divergence. Again, relatively large collimation and focusing (collection) lenses are required that limits the interconnect density. The guided-wave optical backplane interconnection uses optical waveguides (ion-exchanged glass waveguides, silica-on-silicon waveguides, or polymer waveguides) can offer high optical interconnect line density. It, however, suffers from the critical waveguide input and output couplings and the relatively high coupling power loss. Recently, fiber ribbons (another version of guided-wave interconnects) have been utilized for board-to-board interconnection. The fiber ribbons offer excellent beam transmission from optical transmitter arrays to receiver arrays. The

interconnect density is set by the fiber to fiber spacing that is typically 250  $\mu\text{m}$ . The fiber ribbon interconnects do not offer cross-over optical beam interconnection. The optical advantage of cross-over interconnection with no crosstalk is not utilized. The interconnection pattern reconfiguration is not possible.

It would be desirable that the optical interconnects can have simultaneously the advantages of free space interconnects (allow cross over interconnects with no crosstalk, easier interconnect pattern reconfiguration, and low optical propagation and coupling loss) and the advantages of guided-wave (waveguide or fiber) interconnects (high interconnect line density). The basic requirement is providing free space interconnect beams with little beam divergence and with small beam size. Such contradictory requirement for a conventional Gaussian beam is however possible with a non-diffracting beam.

### 1.1 Proposed Concept

New Span Opto-Technology Inc. and University of Miami proposed in Phase I high-density optical interconnection based on free space non-diffracting beams. The non-diffracting beam is an optical beam with pseudo-Bessel (non-ideal Bessel) intensity distribution. Figure 1-1 shows an example of a non-diffracting beam intensity distribution. The diffraction contribution of the finite aperture non-diffracting beam permits the beam to propagate in free space for a substantially large distance without significant beam size broadening (or divergence). A comparison of the non-diffracting beam propagation and Gaussian beam propagation is given in Table I with the same starting beam size of 100  $\mu\text{m}$  (central lobe). Clearly, the non-diffracting beam with 22 small side-lobes can propagate over distance of 40 cm maintaining the similar beam size while the 100  $\mu\text{m}$  Gaussian beam is broadened to over 3225  $\mu\text{m}$  size after the same propagation distance. We consider 40 cm propagation distance because most commercial multi-board computing units have a board-to-board distance within such range. The non-diffracting beam size can be reduced when the maximum interconnect distance is reduced. Using the non-diffracting beam it is equivalent to confine a free space beam in a small beam size within a set propagation distance. Such free space "confinement" allows the free-space beam to have the advantages of the guide-wave propagation (small beam size over a large distance). High-density optical interconnection is thus possible for the free space beams while preserving the advantages of free-space interconnection mentioned above.

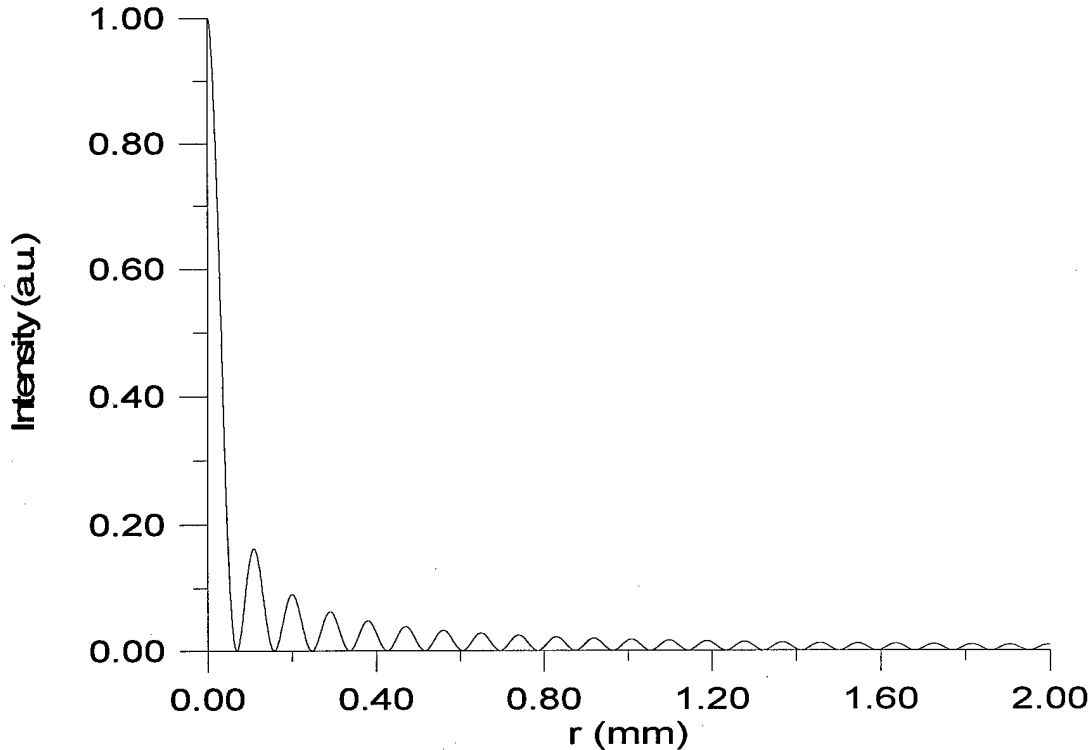


Figure 1-1  
Intensity distribution of a non-diffracting beam in the radial direction  $r$ .

Table I Comparison for the beam diverging property between the conventional Gaussian beam and the non-diffracting beam.

Propagation Distance (cm)		0	10	20	30	40
Beam Size at $e^{-2}$ (full width) ( $\mu\text{m}$ )	Gaussian Beam	100	812	1615	2420	3225
	Non-diffracting Beam (central lobe)	100	97	102	93	105

The finite aperture non-diffracting beam has a beam size of about 4 mm that includes 22 side-lobe rings as shown in Fig. 1-1. High-density non-diffracting beam array can be realized as shown in Fig. 1-2 where the central lobe of each non-diffracting will overlap with some side-lobes of the neighboring beam. This array non-diffracting beam arrangement for optical interconnection is novel and can facilitate the proposed high-density interconnection in free space. With the central lobe carrying data signal and the overlapping side-lobes as crosstalk noise signal, the signal-to-noise ratio is still high since the side-lobes are small. The crosstalk figure is measured in Sec. 2.9. Figure 1-3 shows the comparison of collimated Gaussian beam interconnection and the high-density non-diffracting beam interconnection using the same laser transmitter and photodetector receiver. To allow beam collimation within the 40 cm range, required for most free space or backplane board-to-board interconnection, the Gaussian beam size (diameter) must be about 1 mm (with about 8.7% divergence). This requires a large collimation lens and a focusing lens of about 1 mm size. With the given laser diverging angle of

15°, for example, the distance between the laser and the collimation lens is also large, such as 1.866 mm. Assume a photodetector size of 100  $\mu\text{m}$  for over Gb/s operation, the distance from the focusing lens to the photodetector's sensitive area is about 814  $\mu\text{m}$  at a given focusing angle of 30°. The laser-to-laser spacing must be at least 1 mm. On the other hand, using non-diffracting beam for interconnection the laser-to-laser spacing and the beam central lobe spacing can be set at 250  $\mu\text{m}$ , identical to the spacing of commercially available fiber ribbon. Furthermore, since the central lobe of the non-diffracting beam is less than 100  $\mu\text{m}$  in size, the non-diffracting beam can be directly aligned to the photodetector's sensitive area that is about 100  $\mu\text{m}$  size to eliminate the collection/focusing lens (see Fig.1-3). This greatly simplifies the receiver packaging.

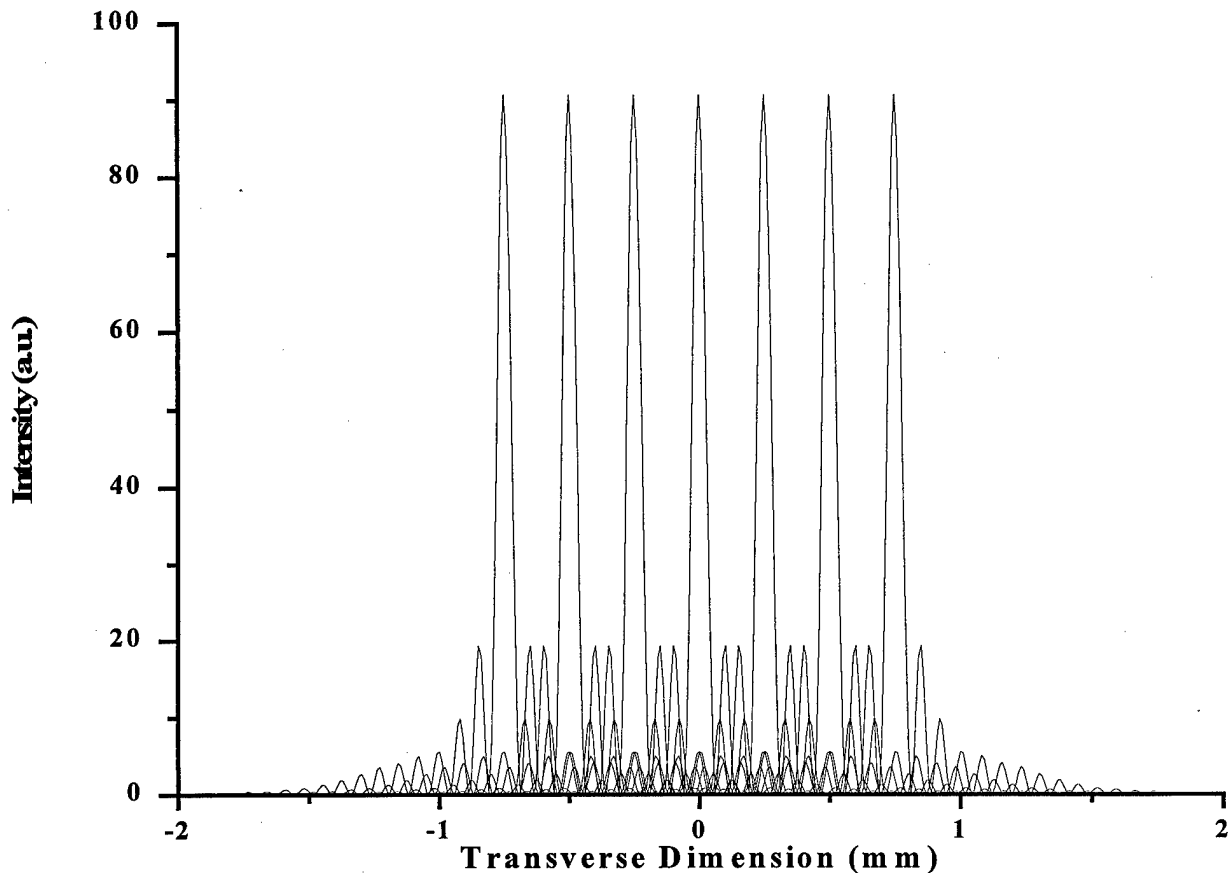


Figure 1-2  
Schematic of non-diffracting beam array intensity distribution showing how high-density interconnect beam arrays can be formed.

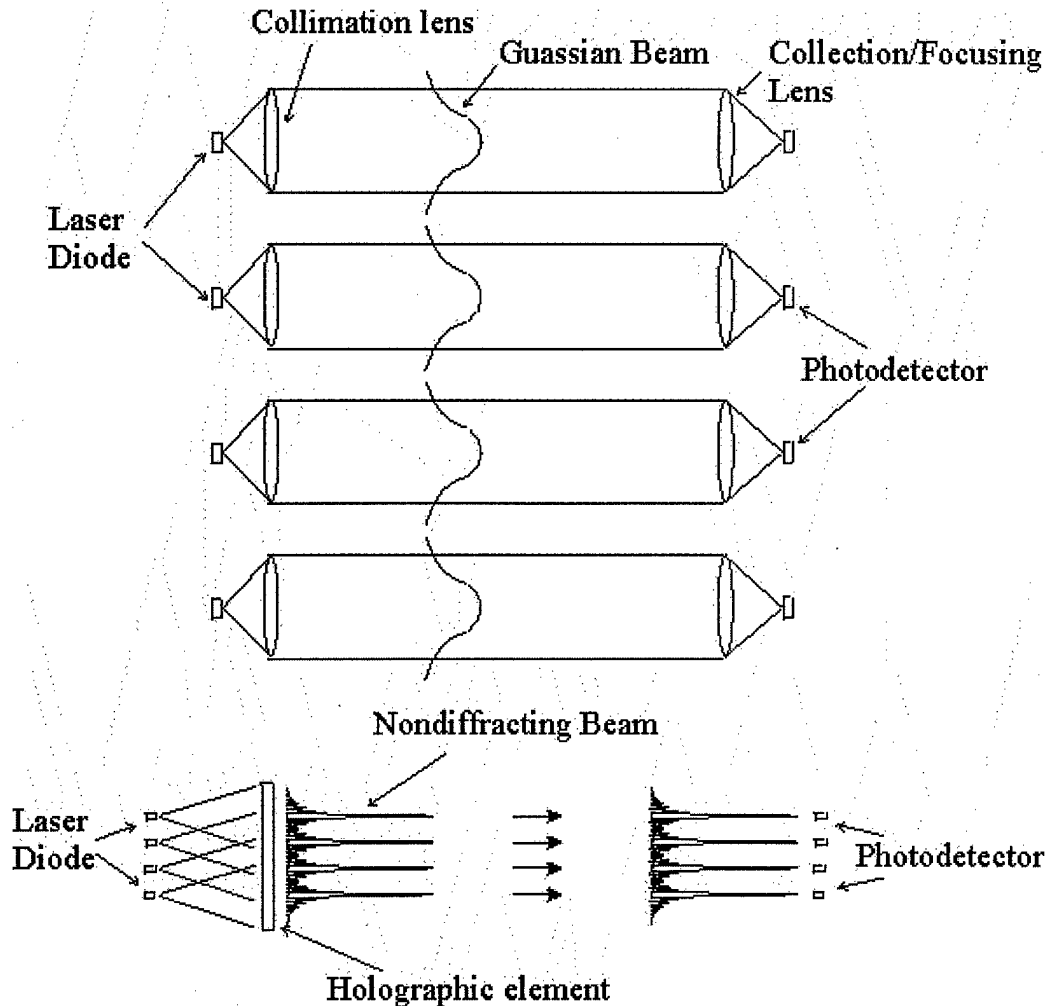


Figure 1-3

Comparison of conventional Gaussian beam interconnection and the proposed non-diffracting beam interconnection. The non-diffracting beam approach facilitates more compact transmitter packaging, high interconnect line density, and eliminates the focusing lenses for the photodetector receiver array making the photodetector packaging easier.

Figure 1-4 shows the architecture of using the non-diffracting beam for high-density board-to-board direct interconnection. Because of the non-diffracting shadowing effect, after the removal of the central lobe by a photodetector the remaining transmitting side-lobes will reform the central lobe after a very short propagation distance (such as 20 mm) beyond the photodetector. Using photodetector arrays with transparent electrodes will facilitate multi-board high-density optical interconnection as shown in Figure 1-4. The non-diffracting beam can also be used for the backplane substrate optical interconnection, as shown in Figure 1-5. Furthermore, the non-diffracting beam approach can be used to form an optical version of "pin" grid array for 3-D packaged multi-chip module (MCM) systems (see Fig. 1-6). The size of the non-diffracting beam is propagation distance dependent. For the interconnection distance of less than 5 cm, the non-diffracting beam size can be as small as 0.5 mm that is about the size of a multimode fiber core. For the interconnection distance of about 40 cm, this is the interconnect distance required in a typical multi-board unit, the non-diffracting beam size is about 4 mm while the central lobe is

only 100  $\mu\text{m}$ . In either case, the non-diffracting beam spacing can be made smaller than or equal to the fiber to fiber spacing (of 250  $\mu\text{m}$ ) in a fiber ribbon. The free space interconnect density can be up to 5 lines per mm or 50 lines per centimeter. Such high optical interconnection density in free space is similar to the density of some polymer optical waveguide interconnects and fiber ribbon interconnects. Consider 2D interconnection array, the interconnection density can be as high as 25/mm<sup>2</sup> or 2500/cm<sup>2</sup>. Such high interconnection density can not be envisioned by using conventional Gaussian beams.

With the high-density free-space interconnection, the interconnection pattern can be reconfigured by conventional free space technique including liquid crystal, electro-optic, photorefractive, holographic, piezoelectric position tuning technologies.

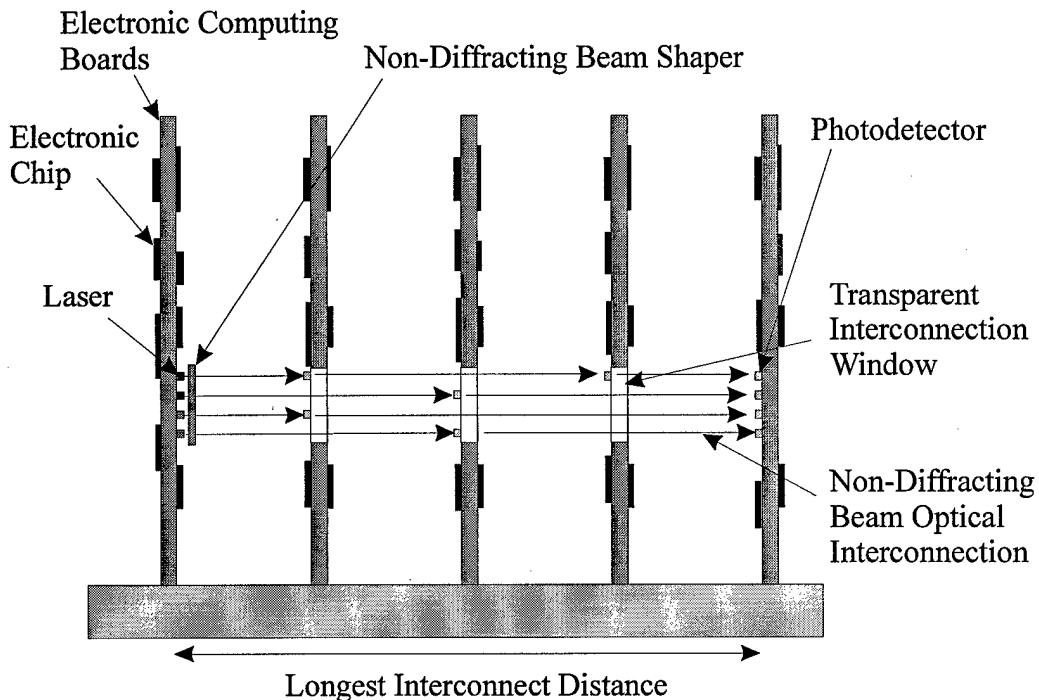


Figure 1-4  
Use of the free-space non-diffracting beam for board-to-board interconnection.

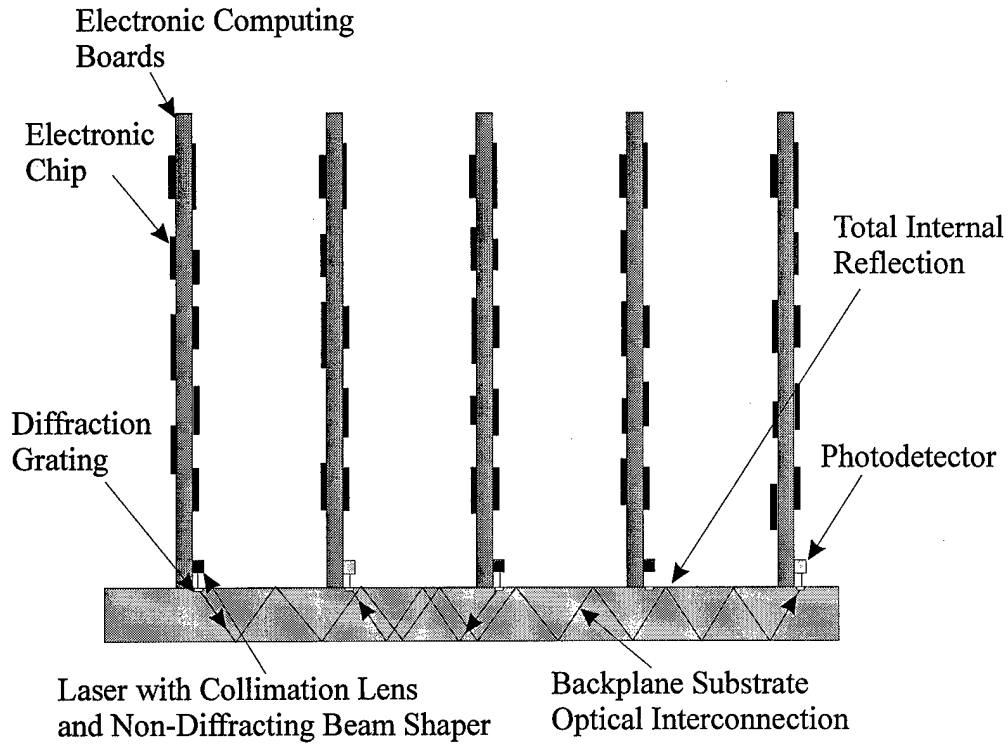


Figure 1-5  
Use of the free-space non-diffracting beam for board-to-board backplane substrate interconnection.

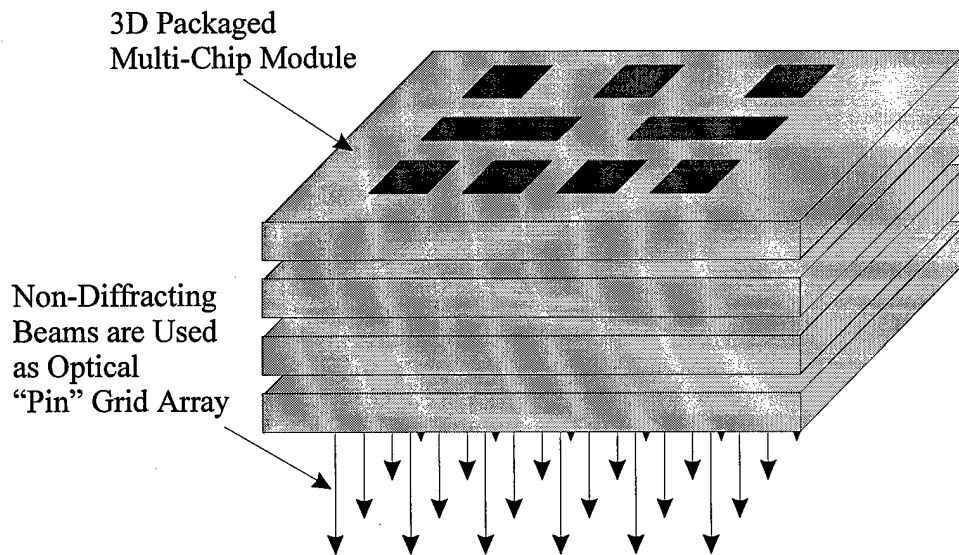


Figure 1-6  
Use of free-space non-diffracting beam for the formation of optical "pin" grid array in a compact 3-D packaged multi-chip module system.



The high-density free-space interconnection concept can also be used for parallel optical computing and optical neural network implementation by generating a high-density two-dimensional optical spot arrays with the non-diffracting beam characteristics.

## 1.2 Summary of Phase I Results

In this Phase I program, New Span Opto-Technology Inc. and University of Miami (subcontractor) demonstrated the feasibility of the proposed high-density optical interconnection based on free space non-diffracting beams. The Phase I results are summarized below.

1. We have examined the existing theory for the non-diffracting beam in terms of beam propagation property and beam size dependence. We have compared the advantages and drawbacks of several existing techniques to realize the non-diffracting beams.
2. We have investigated a new beam-shaping filter that can realize the non-diffracting beam with high efficiency. The beam-shaping filter is a single-element compact diffractive optical component rather than conventional multi-element device.
3. We have demonstrated that the new beam shaping technique can facilitate relatively uniform propagating beam intensity over the required interconnection length. It has a significant advantage over other existing techniques.
4. We further demonstrated that there is no critical optical alignment to achieve the required beam shaping for non-diffracting beam from an incident Gaussian beam.
5. A new non-lithographic laser assisted chemical etching technique demonstrated recently by us has been used to realize the non-diffracting beam shaper.
6. The parameters of the realized non-diffracting beam have been measured and compared to theoretical design values. The measurement includes propagation intensity uniformity, beam intensity profile, and beam forming efficiency. Good agreement between theory and experiment has been demonstrated.
7. The effect of fabrication error has also been accessed.
8. Because of the partial overlapping of the non-diffracting beams for high-density interconnection, a holographic technique has been identified for the formation of high-density non-diffracting beam array.
9. We have set up holographic recording system and recorded holographic optical elements for non-diffracting beam array formation.
10. The performance parameters including efficiency and crosstalk of the holographic array-beam-forming unit have been measured.
11. High-density non-diffracting beam array (with 4 beams per mm density) has been successfully demonstrated.
12. The power budget of the free-space non-diffracting beam array interconnection has been estimated.
13. We further demonstrated the reformation of the non-diffracting central beam after the central lobe is removed by a photodetector. This feature allows the non-diffracting beam

array to be used for cascaded broadcast interconnection to multiple boards using transparent electrodes.

14. The potential applications of the high-density optical interconnection based on free-space non-diffracting beam have been identified.

The overall Phase I work is successful. Detailed results are given below.

## 2.0 RESULTS OF THE PHASE I WORK

### 2.1 Basic Theory of Non-Diffracting Beams

Any wave with a finite aperture in a transverse plane will be subject to diffractive spreading as it propagates outward in free space. In 1987, however, Durnin discovered that the well-known wave equation in free space

$$\left( \nabla^2 - \frac{1}{c^2} \frac{\partial^2}{\partial t^2} \right) \vec{E}(\vec{r}, t) = 0 \quad (1)$$

can have an exact non-Gaussian and non-plane-wave solution described with a field amplitude given by <sup>[18,19]</sup>

$$E(\vec{r}, t) = \exp[i(\beta z - \omega t)] J_0(\alpha \rho) \quad (2)$$

where  $\rho^2 = x^2 + y^2$  and  $J_0$  is the zero-order Bessel function of the first kind. Here  $\alpha$  is the transverse propagation constant in the beam plane (x-y plane) while the  $\beta$  is the propagation constant in z direction. When  $\alpha = 0$  the solution is simply a plane wave. When  $\alpha$  is larger than 0 but smaller than or equal to  $\omega/c$  the solution (Eq. 2) is the so-called non-diffracting beam that has an infinite extend in the transverse plane and is capable of propagating to infinity in z direction without spreading. This means that at every location z the light transverse field distribution is unchanged given by the same  $J_0(\alpha \rho)$ . The non-diffracting beam is thus often called Bessel beam.

The Bessel function  $J_0(\alpha \rho)$  has infinite number of side lobes with a high central peak. Its intensity distribution is shown in Fig.1-1. The intensity distribution of a  $J_0$  beam decays as  $1/\rho$  and is not square integrable. The amount of energy in each side-lobe ring is approximately equal to that in the central lobe. Thus, the exact non-diffracting beam contains infinite amount of energy similar to that of plane wave and is impossible to realize in practical systems. By truncating the infinite extended non-diffracting beam by a soft or hard aperture can realize a pseudo-Bessel (non-exact Bessel) beam that can propagate a substantially large distance without significant beam spreading. Here the soft aperture means the Bessel beam is multiplied by a aperture function that decay gradually to zero while the hard aperture means using an aperture with an abrupt boundary of transmission function. The pseudo-Bessel beam is practical to realize (because of its finite energy) by a variety of techniques including holographic technique, annular slit technique, diffractive optical beam shaping technique, axicon technique, and spatial light modulator technique. Each truncating technique results a pseudo-Bessel beam with different

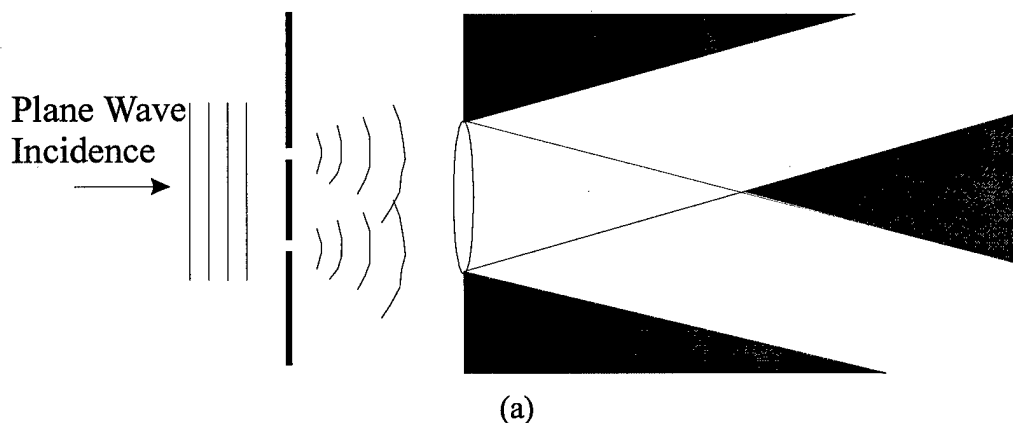
propagation behavior. We summarize the propagation behaviors of these truncating technique in Sec. 2.2 below.

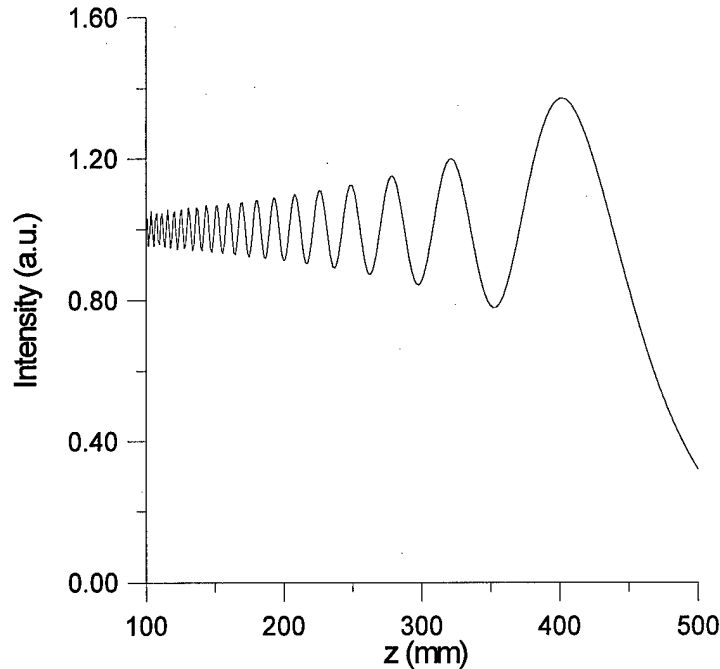
The basic advantages of using (truncated) non-diffracting beam is its ability of maintaining the central lobe for a long propagation range, much longer than that of the Gaussian beam (with beam size similar to the central lobe). Thus, the non-diffracting beam can be used for high-precision autocollimation, optical alignment, optical interconnection, etc.

## 2.2 Summary of Existing Non-Diffracting Beam Forming Techniques and Propagation Behaviors

Truncating the infinite non-diffracting beam with a finite aperture can yield a pseudo-Bessel beam. There are several ways to truncate the infinite non-diffracting beam and each of them results in different pseudo-Bessel beam propagation behavior.

For the pseudo-Bessel beam formed by using an annular slit and a collimation lens<sup>[19]</sup>, as illustrated in Fig. 2-1a with a plane wave incidence, the produced truncated non-diffracting beam has a poor beam forming efficiency due to the thin annular slit. The propagation behavior of such beam is relatively flat in central beam intensity (see Fig.2-1b) with beam intensity fluctuation caused by the hard-aperture truncation either from the lens aperture or from a light block. The central-beam intensity eventually drops due to the end of the shadow region as shown in Fig.2-1a. Using diverging or converging beam incidence can similarly produce the truncated non-diffracting beam<sup>[20]</sup>.





(b)

Figure 2-1

Formation of truncated non-diffracting beam (pseudo-Bessel beam) by using an annular slit and a collimation lens (a). The beam propagation behavior is given in (b).

Fabry-Perot resonator is an alternative technique <sup>[21]</sup> to generate a ring-type beam instead of using the annular slit. Because the ring-type beam is formed by Fabry-Perot interferometry that do not use physical light blocking aperture, the Fabry-Perot resonator approach eliminates the intensity fluctuation on the propagation axis and offers achromatic performance unlike other approaches that depends critically on the light wavelength. However, non-diffracting beam central intensity increases almost linearly (due to the Fabry-Perot resonator behavior) and then drops (due to non-diffracting shadowing).

For the pseudo-Bessel beam formed by using an axicon <sup>[22,23]</sup> with a plane wave incidence, as shown in Fig.2-2a, it gives the required phase delay to form a Bessel beam across the aperture of the axicon. The axicon has a conical surface which is difficult to fabricate to the necessary tolerance. The resulting truncated non-diffracting beam has a linear increase in the central beam intensity along the propagation direction and with intensity fluctuation caused also by the axicon aperture diffraction (see Fig.2-2b). The increase in central beam intensity is due to the fact that the light intersecting the optical axis at any point is incident from a corresponding annular region on the axicon. As the distance from the axicon increases, the annular region size increases that increase the central beam intensity. Thus, the beam is not considered strictly non-diffracting. Again, at the end of the shadow forming region corresponding to the truncated non-diffracting beam propagation length, the central beam intensity drops as expected.

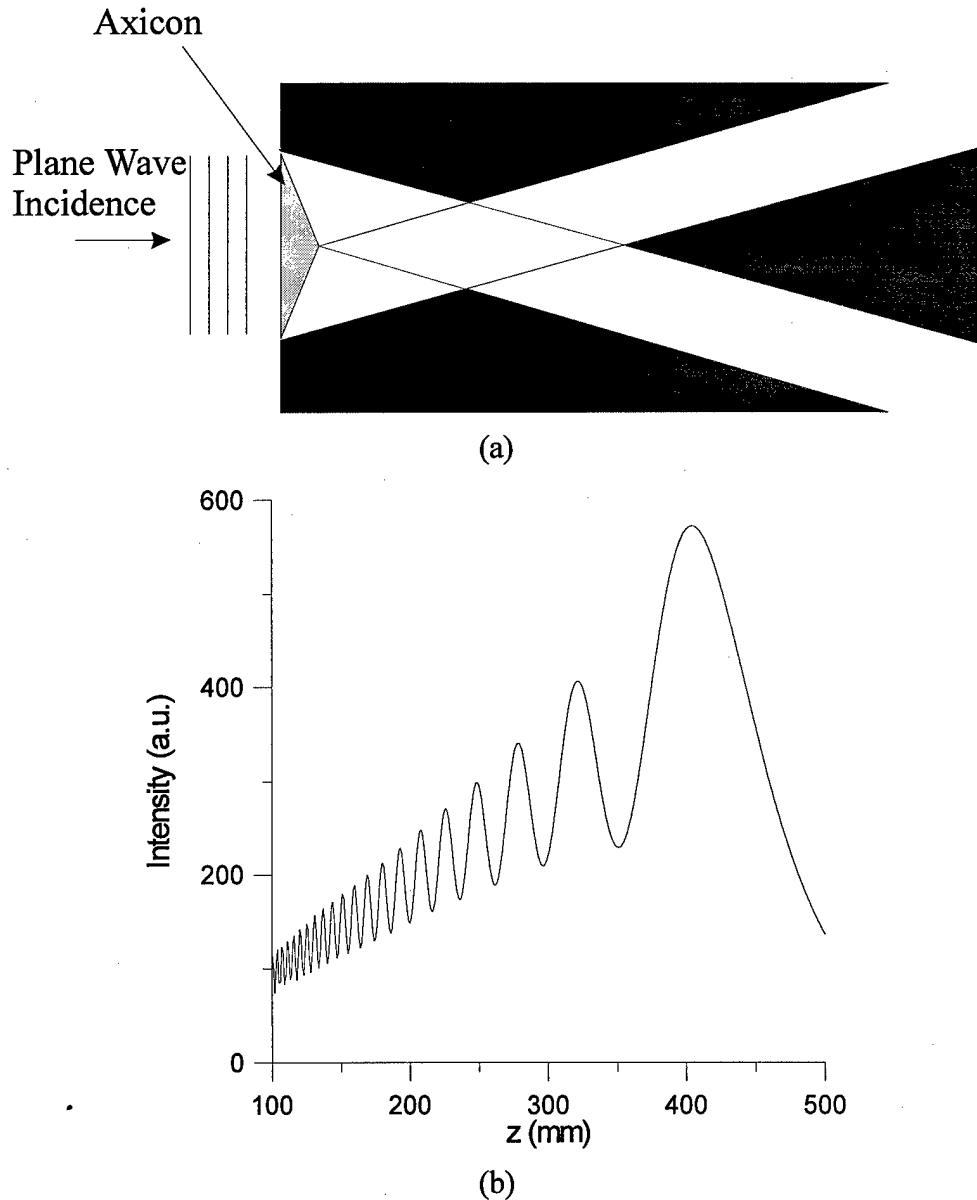


Figure 2-2  
Formation of truncated non-diffracting beam using an axicon (a). The beam propagation behavior is given in (b).

Diffractive optical element (DOE) can be used to simulate the axicon since it is easier to fabricate and offers great flexibility to forming non-diffracting beam from a variety of incident beams including diverging beam and converging beam. Fig. 2-3a shows a DOE that converts an incident Gaussian diverging beam from a laser diode to a non-diffracting beam. The introduction of Gaussian beam intensity distribution offers a soft-aperturing effect to the pseudo-Bessel beam forming when the Gaussian beam size is smaller than the DOE aperture <sup>[24]</sup>. This reduces the central beam intensity fluctuation. Furthermore, since the central Gaussian beam has higher intensity than the outer beam, the intensity contribution to the non-diffracting beam propagation is deviated from that of the linear increasing of the axicon technique. Figure 2-3b shows the

central beam intensity variation as a function of propagation distance. It increases almost linearly first then curves to flat and then drops as the propagation distance increases. This is due to the Bessel-Gauss effect <sup>[25]</sup> that can be explained by the product of the annular region size and the Gaussian intensity distribution. There is no fundamental difference on the propagation behavior of the truncated non-diffracting beam whether the incident beam is a diverging Gaussian beam, a converging Gaussian beam, or even a collimated Gaussian beam. The only difference in these cases is the phase filter design of the DOE. The Bessel-Gauss beam has shorter propagation distance than that of axicon or annular slit technique.

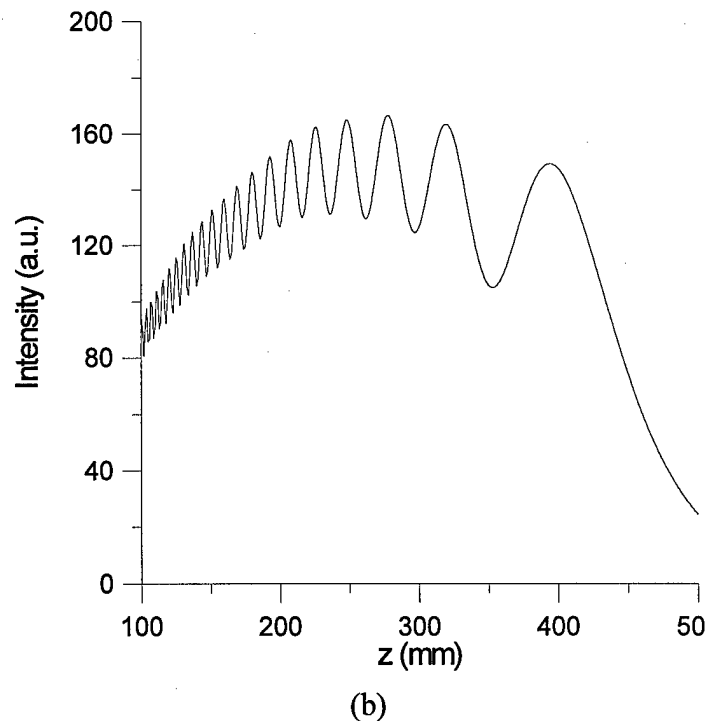
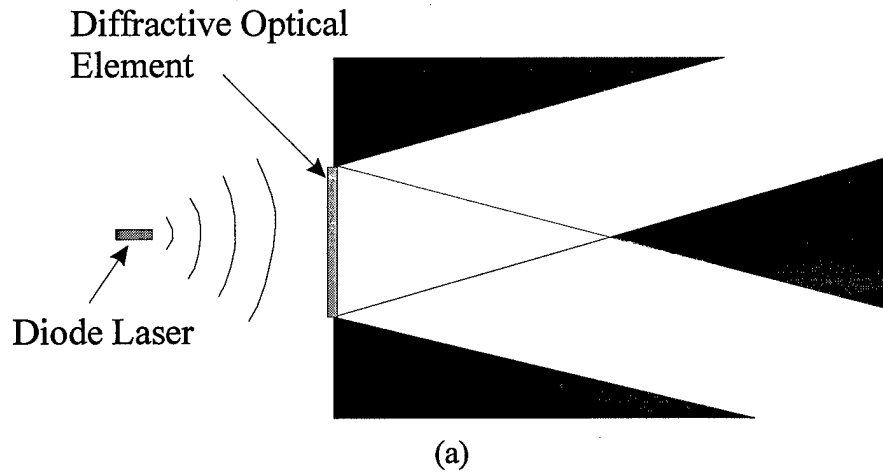


Figure 2-3

Diffractive optical element can be used to form truncated non-diffracting beam from an incident Gaussian beam (a). The corresponding propagation behavior is given in (b).

Other techniques to truncate the Bessel beam have been proposed including modifying the side-lobe intensity for longer propagation distance <sup>[26,27]</sup>, using super-Gaussian beam for a flat intensity distribution <sup>[28]</sup>, and using reflective holographic optical element (binary diffractive element) <sup>[29]</sup>. Modifying side-lobe intensity distribution makes the beam size larger. Using super-Gaussian beam to truncate the Bessel beam is equivalent to using a hard aperture (softer than a light block). The realization of the original Bessel beam before the truncation is still a problem discussed above. Using reflective holographic optical element is similar to that of transmissive diffractive optical element technique mentioned above.

The key requirements to optical interconnect are that (a) the beam has minimal divergence within the interconnection distance, (b) the central beam width is small enough to eliminate the needs for focusing lens at the receiving photodetector, (c) the intensity of the non-diffracting beam central peak is relatively flat within the propagation range, (d) there is reduced intensity fluctuation of the central beam peak, and (e) there is high truncated non-diffracting beam forming efficiency. With proper design, any of above techniques can satisfy the requirements (a) and (b). The annular slit technique can satisfy requirement (c) but not (d) and (e) (with efficiency less than 1%). The axicon technique can satisfy requirement (e) but not (c) and (d). The conventional DOE technique can satisfy requirements (d) and (e), but not (c). Modified side-lobe technique proposed by Rosen <sup>[26]</sup> has a very large beam that can not be considered.

To achieve a uniform intensity along the propagation direction (requirement (c)) and high efficiency (requirement (e)), two phase-only computer generated holograms have been proposed and used for the non-diffracting beam forming <sup>[30]</sup>. One element transforms the incident uniform intensity distribution (plane wave) to a  $1/r$  intensity distribution while the other element combines the correction of the phase distortions from the first element and the desired conical phase transformation. This technique is to appodize the incident beam by a factor of  $\frac{1}{r}$  (or  $\frac{1}{\sqrt{r}}$  in light amplitude) using a conical phase transmission function

$$t(r) = \frac{1}{\sqrt{r}} \exp\left(\frac{i2\pi r}{r_0}\right), \quad r \leq R$$

$$= 0, \quad r > R$$
(3)

where  $R$  is the radius of the element and  $r_0$  is a constant that determines the size of the central spot of the Bessel beam. The diffraction integration of the conical phase function in a cylindrical coordinate using a common cylindrical symmetry axis yields the required truncated Bessel beam intensity distribution perpendicular to the axis. This non-diffracting beam forming technique is attractive since the efficiency can approach 100% using thick dichromatic gelatin hologram. However, they only demonstrated efficiency of about 10.5% for each element using Lee-type binary computer-generated holograms. The major problem of this technique is the critical optical alignment and positioning of the two computer-generated holograms that makes the non-diffracting beam forming unit less compact and subject to vibration sensitivity. Furthermore, the demonstrated technique applies only to plane wave incidence rather than a practical diverging Gaussian beam from a laser diode.

## Our Non-Diffracting Beam Forming Technique

Our design and implementation for non-diffracting beam forming consider a single diffractive optical element. It is a new beam forming approach with simultaneous advantages of high efficiency, compactness (single element), applicable to diverging Gaussian beam, relatively small intensity fluctuation, and relatively flat central peak intensity distribution over the propagation range. It can satisfy all (a) to (e) non-diffracting beam requirements mentioned above. Details are given below.

### 2.3 Design of Beam Shaping Element

We designed a phase-only beam-shaping filter to transform a Gaussian beam into a nondiffracting beam with constant axial intensity distribution within the propagation distance of 40 cm. The central spot diameter of the formed nondiffracting beam was about 130  $\mu\text{m}$ . Thus the corresponding  $e^{-2}$  full width of the central spot was 95  $\mu\text{m}$ , which is around the diameter of sensitive area of most of detectors. The maximum propagation distance of nondiffracting beam can be estimated by

$$z_{\max} = R \cdot \left[ \left( \frac{2\pi\rho}{2.405\lambda} \right)^2 - 1 \right]^{1/2} \quad (4)$$

where  $R$  is the radius of the beam-shaping filter,  $\rho$  is the radius of the central spot, and  $\lambda$  is the wavelength. We chose  $R$  to be 2 mm, so the maximum propagation distance is 53.6 cm. However, the equation above is given by the geometrical law for nondiffracting beam formed by plane wave incidence on classical axicon, taking no account of diffraction and intensity distribution of incident beam. From the calculation of Fresnel diffraction integral later in this section, it can be seen that in fact the maximum propagation distance is about 45 cm.

Based on the geometrical law of energy conservation, we calculated the desired phase transmittance function of the filter. Suppose the transverse intensity distribution of the input Gaussian beam is

$$P_o(r) = P_0 \exp(-2r^2 / w^2) \quad (5)$$

where  $r$  is the distance from the optical axis,  $w$  is the width of the beam. The longitudinal axial intensity distribution of the output nondiffracting beam between  $z = d_1$  and  $z = d_2$  is

$$P_z(z) = c = \text{const} \quad (6)$$

where  $z$  is the distance from the filter. Applied the geometrical law of energy conservation, the transmittance function  $t(r) = \exp[ik\psi(r)]$  is determined by



$$\begin{aligned}\frac{d\psi(r)}{dr} &= -r/[r^2 + z^2(r)]^{1/2} \\ z(r) &= d_1 + a[1 - \exp(-2r^2/w^2)] \\ a &= \frac{P_0\pi}{2c}w^2 = \frac{d_2 - d_1}{1 - \exp(-2)}\end{aligned}\quad (7)$$

Here we chose  $w = 2\text{mm}$ ,  $d_1 = 0$ ,  $d_2 = 50\text{ cm}$ . The computed phase transmission function of the filter is shown in Fig. 2-4. Fig. 2-5 shows the on-axis intensity distribution of the output nondiffracting beam calculated by Fresnel diffraction integral.

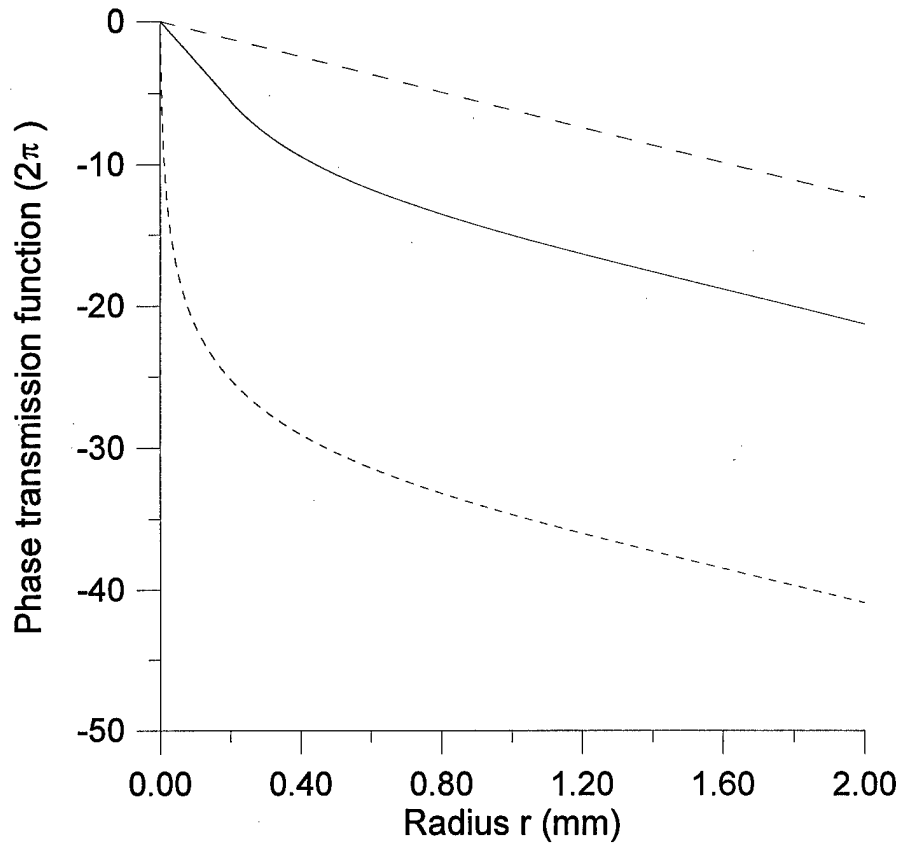


Figure 2-4

Computed phase transmission function of filters for forming a nondiffracting beam. Lower dash line is corresponding to  $\psi(r)$  calculated by using the geometrical law of energy conservation <sup>[31]</sup>.

Solid line is our beam shaping phase function  $\psi_n(r)$ . Top dash line is corresponding to the classical axicon.

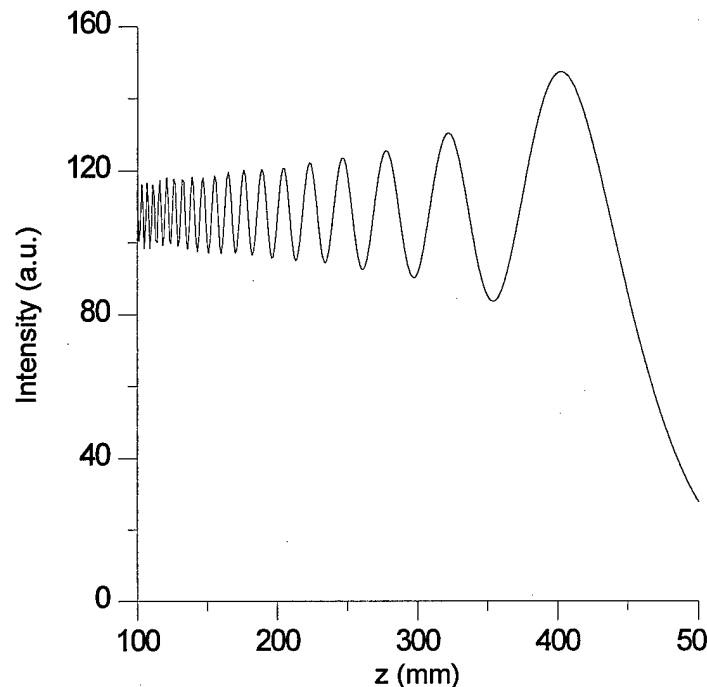


Figure 2-5

On-axis intensity distribution of the nondiffracting beam transformed from a collimated Gaussian beam by the filter with phase transmission function  $\psi(r)$  calculated by geometrical law of energy conversion<sup>[31]</sup>.  $z$  is the distance from the filter.

Compare Fig 2-5 with Fig. 2-2(b) and 2-3(b), it can be seen that the intensity as a function of  $z$  is now constant within the maximum propagation range of about 45 cm, aside from the local fluctuation. The local Fresnel fluctuation is not as large as the beam demonstrated by two-element technique<sup>[30]</sup>. The new design avoiding the linear growth of the classical axicon can be explained in the following intuitive way. As shown in Fig 2-4, the phase transmission function of the new beam-shaping filter is sharper than the classical axicon within the inner part of the filter, and they are approaching to the axicon phase distribution for the outer part. For the classical axicon, the neighborhood of a point at a distance  $z$  along the optical axis receives light mainly from a thin annulus in the filter plane. The radius and the area of the annulus, and thereby its energy contribution, are all proportional to  $z$ . Meanwhile, for the new filter with Gaussian beam incidence, The relatively flat intensity at large  $z$  is believed to be caused by Gaussian intensity correction that reduces light intensity in each thin annulus as radius increases on the filter. This explanation is in consistent to that shown in Fig. 2-3(b) by Bessel-Gauss effect. The relatively flat intensity distribution at smaller  $z$ , that is not possible by Bessel-Gauss effect, is made possible by the sharper phase transmission function at smaller radius that increases the light concentration with a larger corresponding annulus area for each neighborhood  $z$ . Based on the similar argument the phase function, lower dashed curve of Fig. 2-4 calculated by geometrical law of energy conversion<sup>[31]</sup>, can similarly produce a relatively flat intensity distribution within the propagation range.

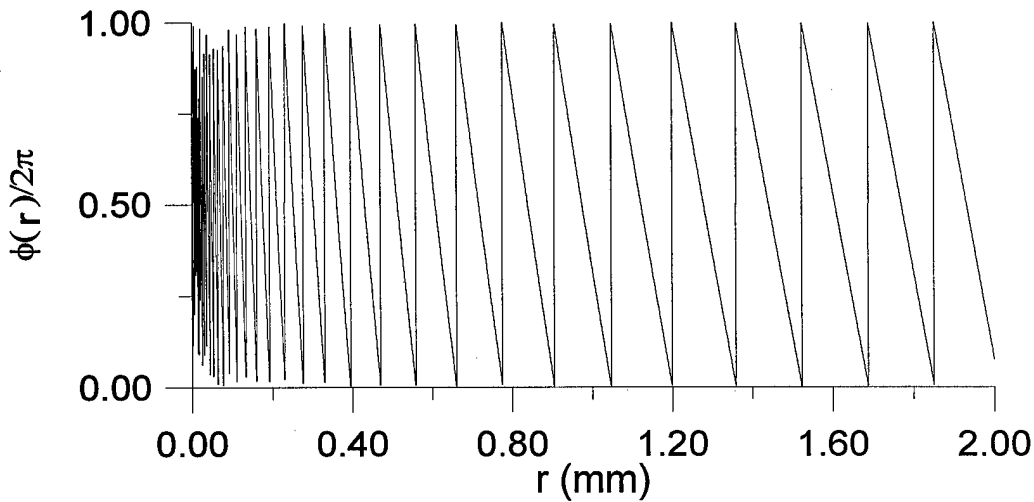
For the phase transmission function  $\psi(r)$ , adding or reducing  $2\pi$  makes no difference. Therefore, we have the complex transmission function  $t(r) = \exp[i\phi(r)]$ , where

$$\begin{aligned} \phi(r) &= \psi(r) + 2m\pi \\ 2m\pi &\leq \psi(r) \leq (2m+1)\pi \end{aligned} \quad m \text{ is an integer.} \quad (8)$$

As shown in Fig. 2-7(a), the function  $\phi(r)$  corresponding to the lower dash curve of Fig. 2-4 oscillates very quickly in the range of  $r < 0.2mm$ . It even oscillates between 0 and  $2\pi$  within  $1 \mu m$  in the area very near the center of the filter. So it is hard to fabricate a real element with such a phase transmission function. This problem is caused by the original phase transmission function  $\psi(r)$  shown in Fig. 2-4 (lower dashed curve) is too sharp when radius is small. However, we found that if we changed the slope of  $\psi(r)$  for  $r < 0.2mm$  to be the same value as  $r = 0.2mm$ , the on-axis intensity of the formed nondiffracting beam would not changed much (see solid curve of Fig.2-4). The new phase transmission function  $\psi_n(r)$  is given by

$$\begin{aligned} \psi_n(r) &= \psi(r = 0.2mm) - \left. \frac{d\psi(r)}{dr} \right|_{r=0.2mm} \cdot (0.2mm - r) + const, & r < 0.2mm \\ \psi_n(r) &= \psi(r) + const, & r \geq 0.2mm \end{aligned} \quad (9)$$

while its  $\phi(r)$  is shown in Fig. 2-6(b). Calculated from Fresnel diffraction integral, the on-axis intensity distribution of the output beam formed by this new filter from incident collimated Gaussian beam is shown in Fig. 2-7. We can see that it is almost the same as Fig. 2-5. Fig. 2-8 is the calculated transverse intensity distribution of the formed beam at different distance from the filter. It can be seen that the diameter of the central spot size of the beam is about  $130 \mu m$ , kept almost the same at the three positions. This demonstrates that the formed beam is a truncated nondiffracting beam with negligible beam spreading within 40 cm propagation range. It satisfies the design requirement. As shown in Fig. 2-6(b) now the sharpest zone of the desired phase pattern  $\phi(r)$  becomes larger than  $35 \mu m$ . Since our fabrication system can make relief surface of different depth with the width of  $1 \mu m$ , it is possible to make such a filter as a quasi-continuous phase-only element. The efficiency of the non-diffracting beam shaper can approach 100%.



(a)

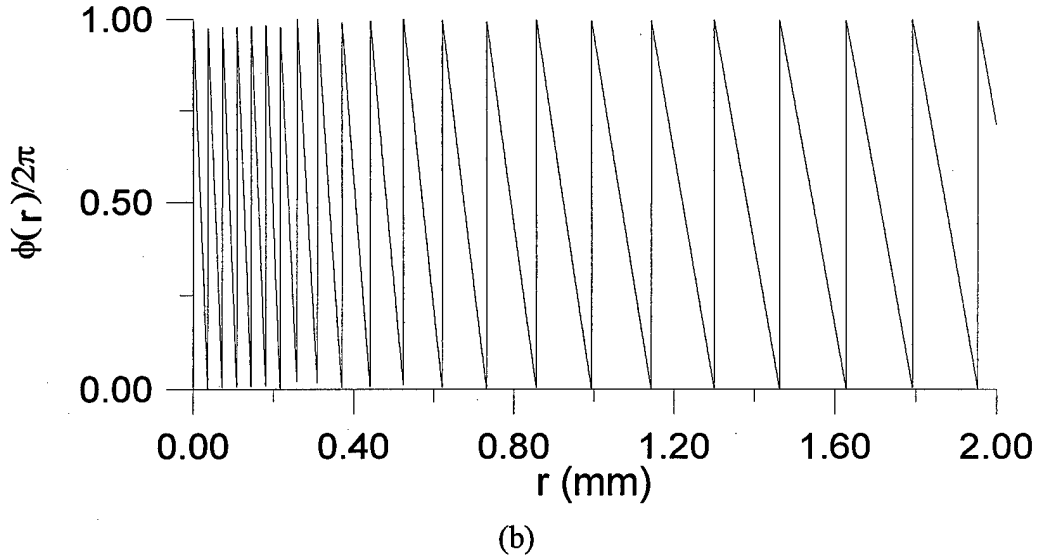


Figure 2-6

The phase pattern  $\phi(r)$  of the nondiffracting beam-shaping filter. (a)  $\phi(r) = \psi(r) + 2m\pi$ . (b)  $\phi(r) = \psi_n(r) + 2m\pi$ .

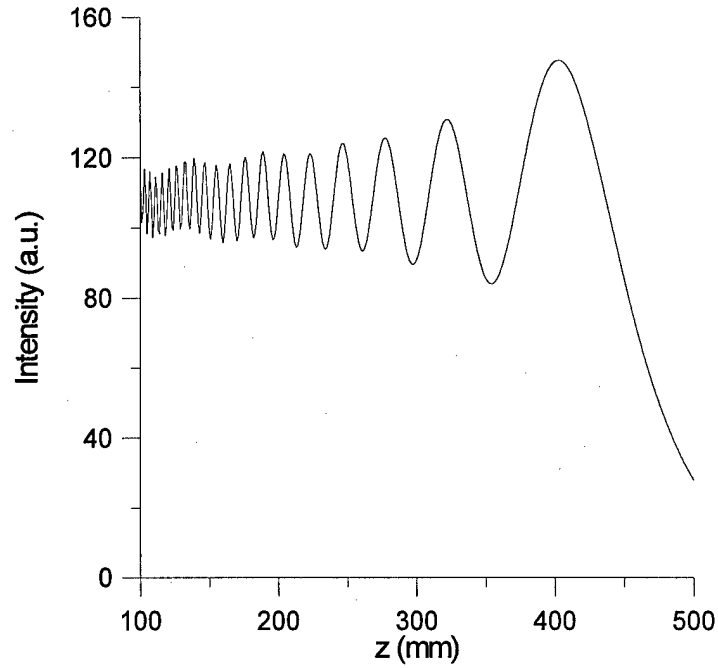


Figure 2-7

On-axis intensity distribution of the nondiffracting beam transformed from a Gaussian beam by our new filter with phase transmission function  $\psi_n(r)$ .  $z$  is the distance from the filter.

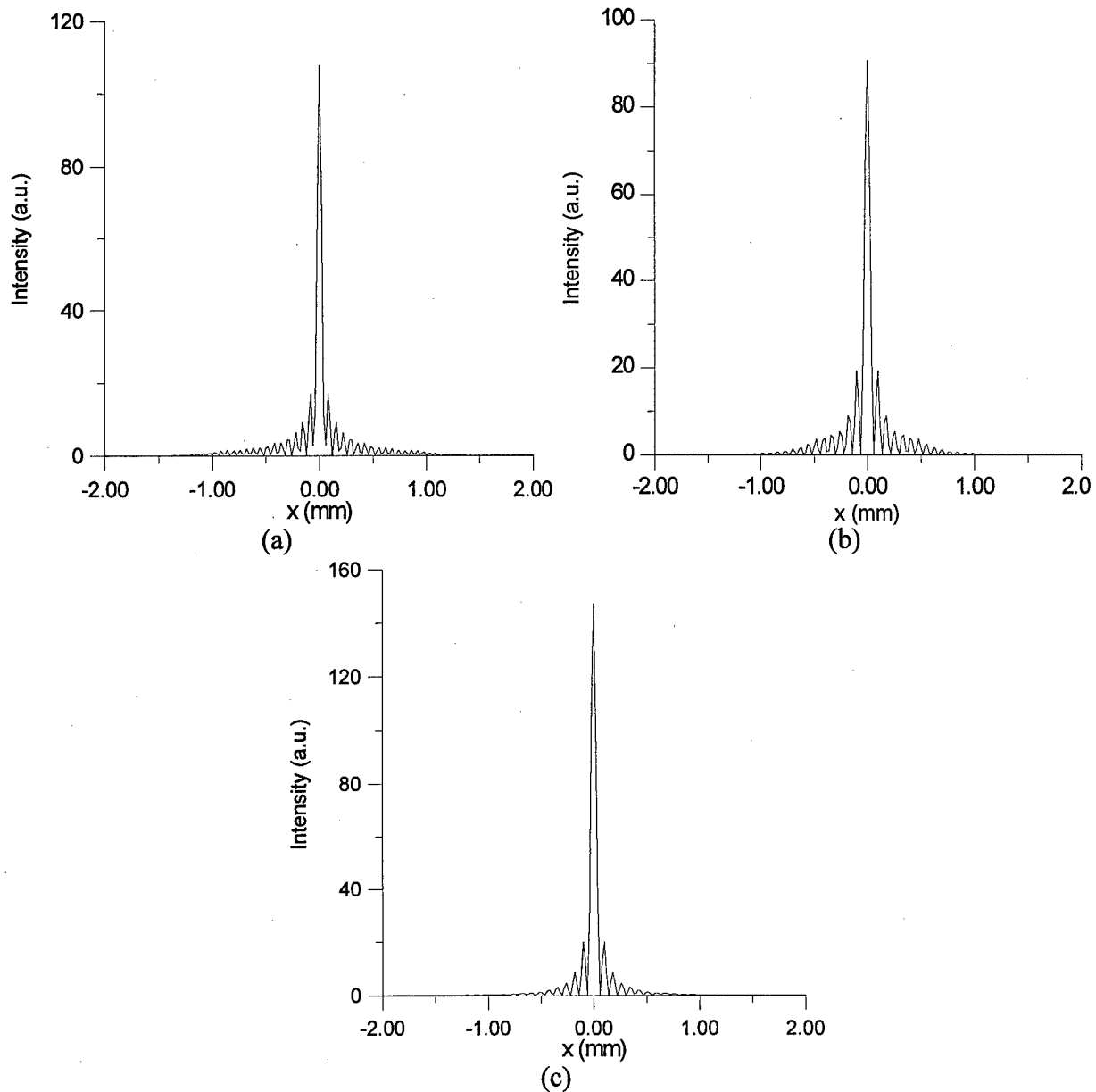


Figure 2-8

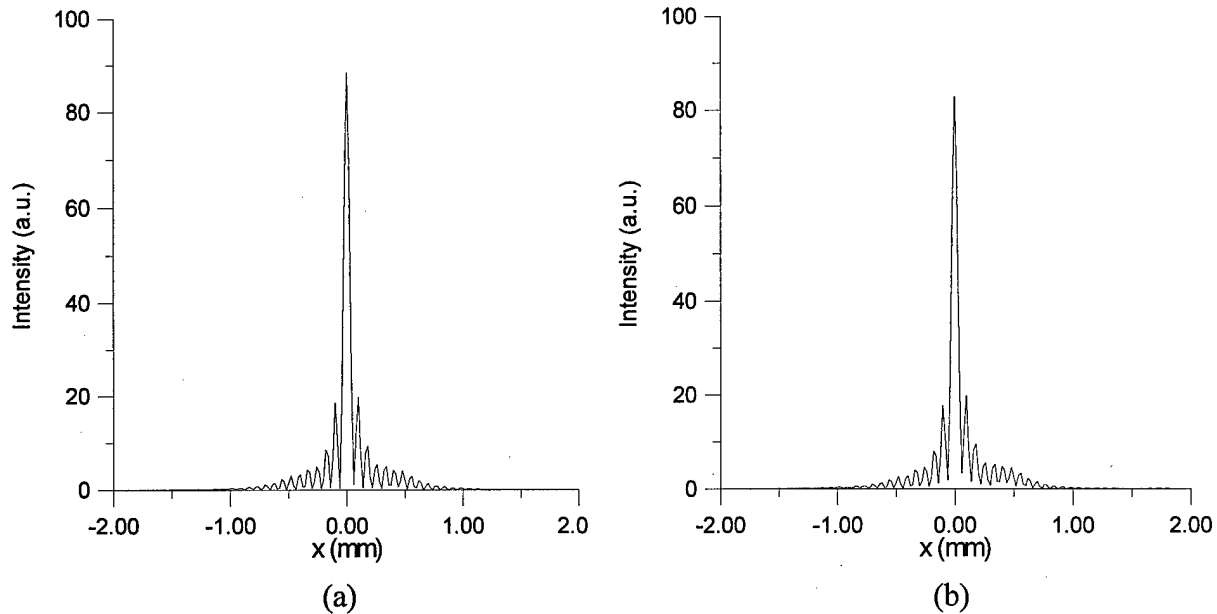
Calculated transverse intensity distribution of the formed beam at different distance from the filter: (a) 20 cm, (b) 30 cm, (c) 40 cm.  $x$  is the transverse coordinate position across the beam center.

#### 2.4 Effect of Misalignment and Incident Beam Size to Shaped Non-Diffracting Beam Quality

The theoretical design presented above is attractive in several ways. First, it demonstrates that a single diffractive optical element can achieve high-efficiency non-diffracting beam forming. Second, it introduces a simple phase filter pattern that can be practically realized by our gray-level mask and one-step etching technique, to be detailed in Sec. 2.5. Third, it demonstrates that the central beam has a reasonably flat intensity distribution over the interconnection range.

Two additional factors on the non-diffracting beam forming should be considered and discussed. They are the effect of misalignment between the incident collimated Gaussian beam and the DOE beam shaper and the effect of the incident beam size variation. To consider these effects we assume the default beam shaper size and the incident Gaussian beam size are identical to the design values given in Sec. 2.3.

The misalignment between the incident Gaussian beam and the beam shaper element will influence the non-diffracting beam shaping quality. Figure 2-9 shows the intensity distribution of the non-diffracting beam across the beam center at the distance of 30 cm from the beam shaper, when the lateral misalignment between the incident Gaussian beam and the beam shaper is 0.25 mm, 0.50 mm, 0.75 mm, and 1.00 mm, respectively. The misalignment induces asymmetry to the non-diffracting beam side-lobes while the position and width of the central spot are kept almost the same. The misalignment also causes slight drop in central peak intensity. The effect of misalignment to side-lobes is not distinguishable until the lateral misalignment is larger than 0.5 mm or 500  $\mu\text{m}$ . Thus, the proposed new beam shaping technique for non-diffracting beam is not sensitive to slight incident beam misalignment.



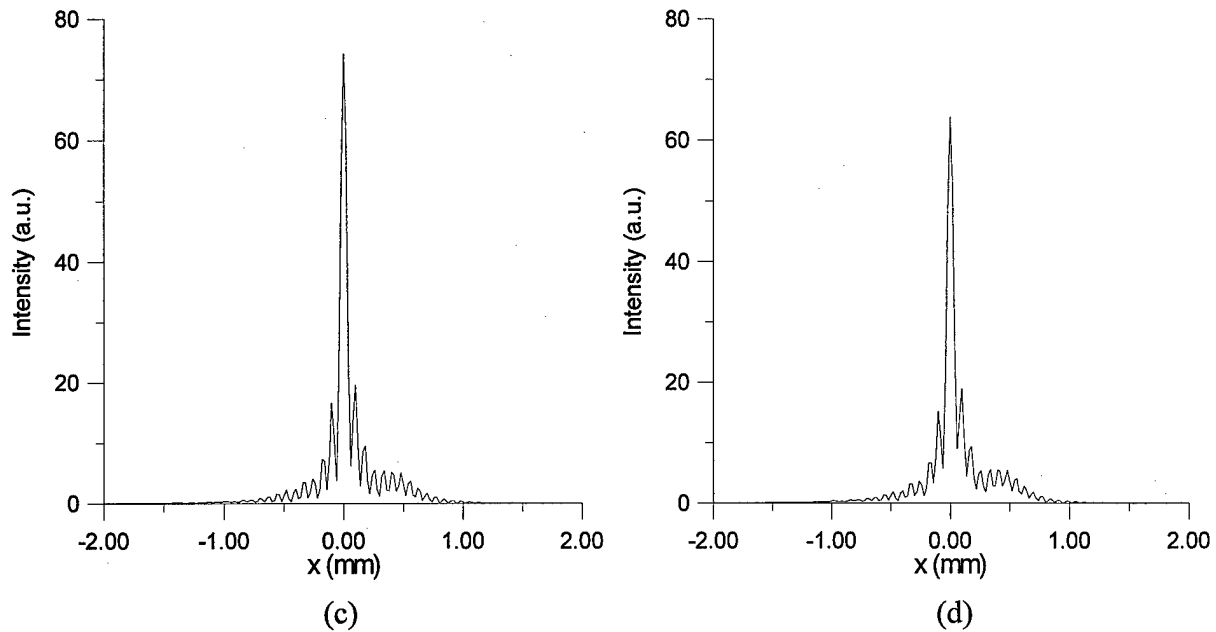


Figure 2-9

The intensity distribution of the non-diffracting beam across the beam center at the distance of 30 cm from the beam shaper, with the lateral misalignment between the incident collimated Gaussian beam and the beam shaper as (a) 0.25, (b) 0.50, (c) 0.75, and (d) 1.00 mm, respectively.

The variation of the incident Gaussian beam size will also affect the beam forming quality and beam propagation behavior. Let the actual laser beam waist be  $(1+\delta)w$  with  $w$  as the design Gaussian beam width and  $\delta$  as the relative error. The effect of 25% beam size error, smaller or larger, to the shaped beam intensity distribution at 30 cm from the beam shaper is given in Fig. 2-10. Clearly, there is no significant difference on the beam transverse intensity distribution as compared to the design distribution caused by such error. We notice only a slight change in the central peak height that is lower when the incident beam size is smaller while higher when the incident beam size is larger. This is in part due to the fact that larger incident Gaussian beam has a higher total energy within the total beam shaper aperture when we normalized Gaussian peak intensity. Although the transverse beam intensity distribution shows little variation by such error, based on our visual observation, the minor variation in side lobes does contribute significantly to the non-diffracting beam propagation behavior. Figure 2-11 shows the corresponding on-axis intensity distribution of the beam along the propagation direction  $z$ . Excluding the local fluctuations caused by the known aperture diffraction, the intensity decreases along the propagation direction when  $\delta = -0.25$ , while it increases within the maximum propagation distance when  $\delta = 0.25$ . The ideal propagation behavior is given earlier in Fig. 2-7 when  $\delta$  is 0. When the incident beam waist is smaller than the designed value the effective aperture of the beam shaper is smaller and the shaped beam could not maintain a flat intensity distribution. The diverging contribution is more than the converging contribution even at a shorter propagation distance. This results in earlier lowering of the peak intensity. When the incident beam waist is larger there is higher side-lobe intensity that increases converging contribution. Using the similar annular region concept, that was used to describe the intensity increasing behavior of beam forming by an axicon, it is not difficult to understand that the intensity increasing behavior when increasing incident beam size. In fact further increasing of the incident beam size will result in

propagation behavior approaching that of the plane wave shown in Fig.2-11c. The intensity distribution is found to grow within the maximum distance but the growth is not as quickly as in the case of using classical axicon. Our calculation indicates that for beam size error whin 6% the average on-axis intensity distribution (excluding the local fluctuation) varies within 10%, smaller than the fluctuation, and is considered acceptable.

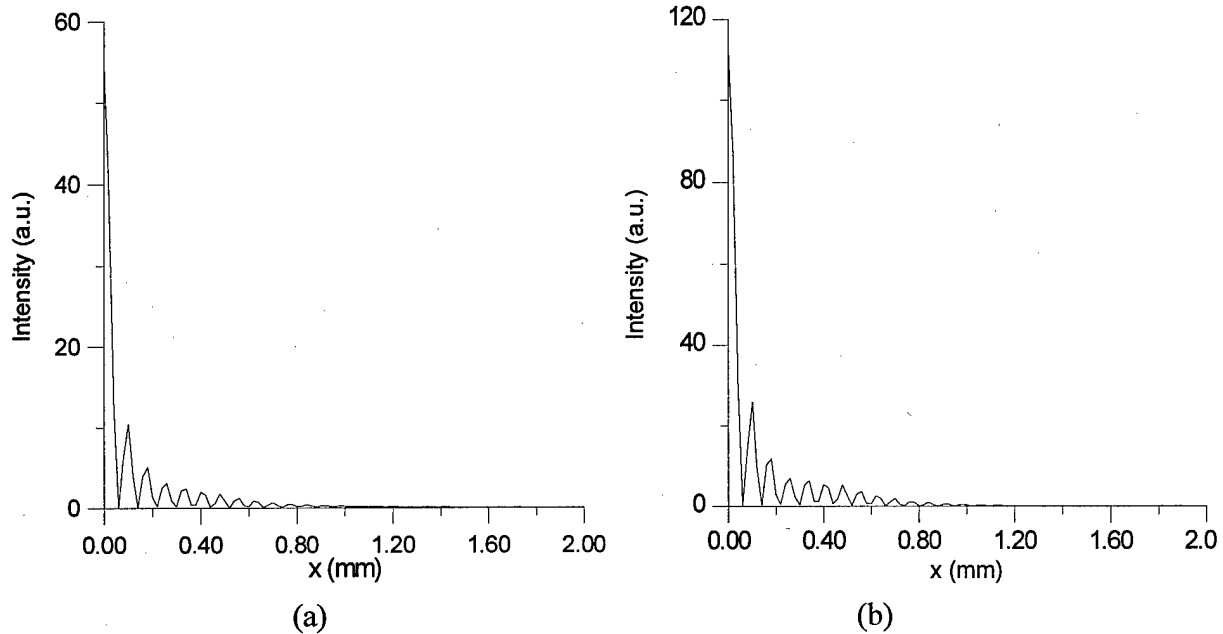
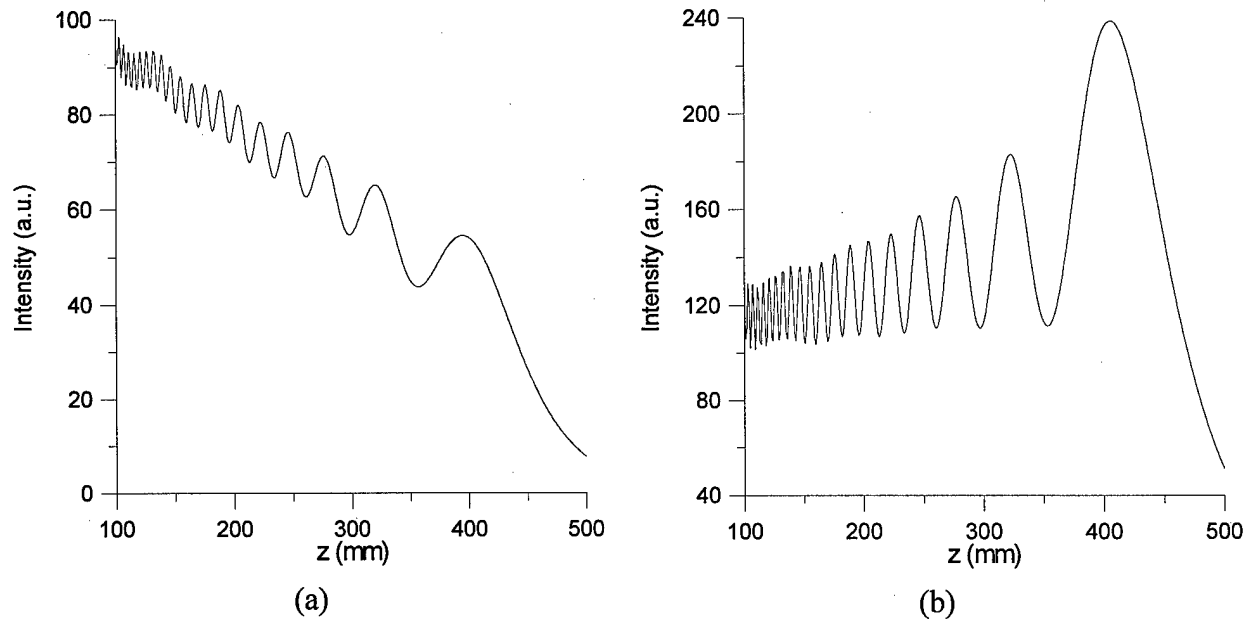


Figure 2-10

The intensity distribution of the nondiffracting beam across the beam center at the distance of 30 cm from the beam shaper, with  $\delta$  equal to (a) -0.25 and (b) 0.25. The comparison can be made with the ideal beam size case ( $\delta = 0$ ) presented in Fig. 2-6.





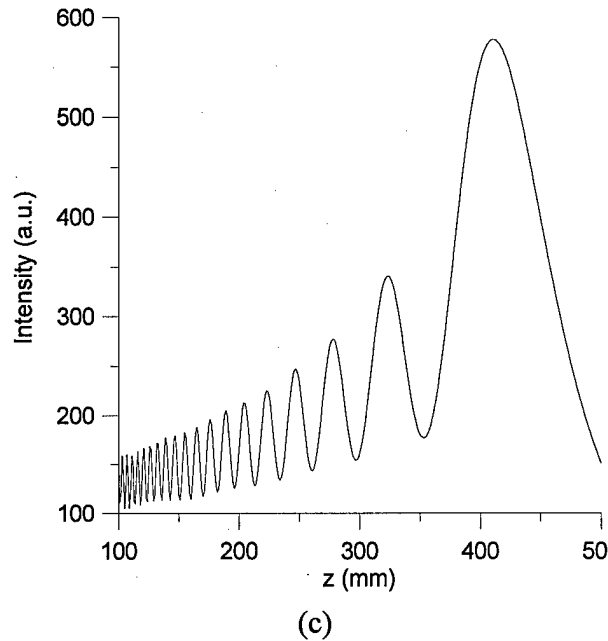


Figure 2-11

The on-axis intensity distribution of the beam along the propagation direction  $z$  when (a)  $\delta = -0.25$ , (b)  $\delta = 0.25$ , and (c) in plane-wave incident case. The comparison can be made with the ideal incident beam size case presented in Fig. 2-7.

## 2.5 Non-Lithographic Fabrication of the Beam Shaping Element

The beam-shaping element for the formation of the truncated non-diffracting beam is a diffractive optical element (DOE). It is a circular phase filtering element with the phase function calculated in Sec. 2.3 and illustrated in Fig. 2-4. The continuous phase pattern can be realized by using surface relief structures with many phase levels. The more the phase levels the better it simulate the continuous phase pattern.

The fabrication of such phase filter element can use conventional DOE fabrication process namely binary multi-mask-and-etch process as shown in Fig.2-12. Such fabrication process requires many binary photo masks and many alignment, photoresist coating, photoresist developing, and surface etching steps. The fabrication is alignment sensitive, low yield rate, and costly. The line resolution of the DOEs depends largely on the photolithographic patterning, coating, processing, and etching techniques. The fabrication constraints limit the number of phase levels that can be achieved and the DOE maximum diffraction efficiency. Typical number of phase levels achieved by this fabrication technique is 8 and in some case can be 16. This technique is not suitable for continuous surface-relief structure fabrication.

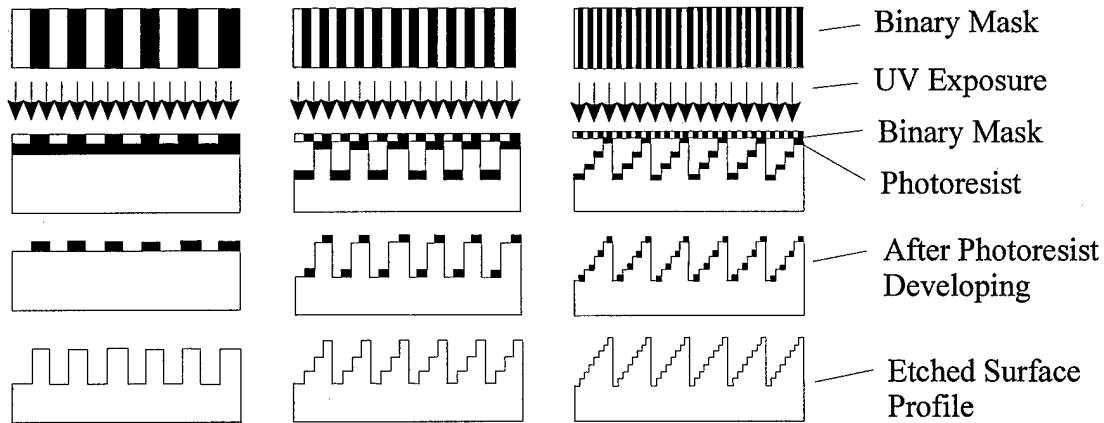


Figure 2-12

Conventional binary multi-mask-and-etch fabrication for diffractive optical element. Such fabrication process is alignment sensitive, low yield rate, and costly.

We have recently demonstrated a laser generation of gray-level mask technique on a silver ion-exchanged high-energy-beam sensitive glass <sup>[32]</sup>. We further demonstrated that the gray-level glass mask can be directly etched in a diluted hydrofluoric acid solution to yield surface relief structure on the glass based on different etching rate on different gray-level regions <sup>[33]</sup>. The transparent laser written region has a higher etching rate than the darker region. By controlling the laser writing parameter and the gray-level pattern distribution, we can achieve the required phase filter in one-step etching, as shown in Fig. 2-13. Etching through the ion-exchanged layer can yield transparent phase-only diffractive optical element. This fabrication is a non-lithographic process and is effective for the beam shaper fabrication. Details on such fabrication technique and the fabrication process are given below.

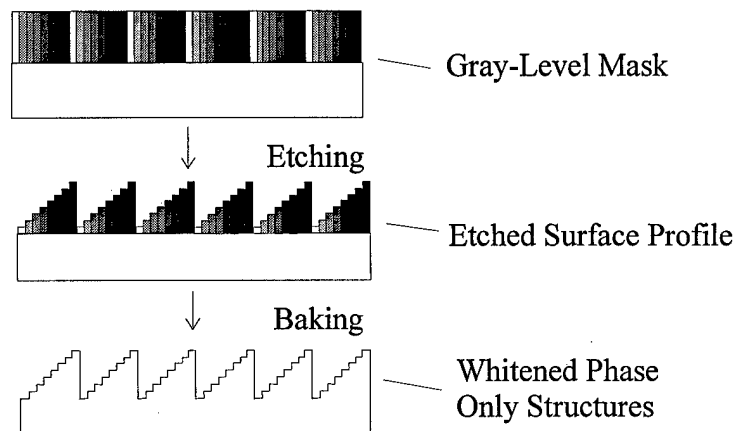


Figure 2-13

Non-lithographic fabrication process for the beam shaper. The process is a laser assisted chemical etching process on an ion-exchanged high-energy-beam sensitive glass.

### 2.5.1 Laser Generation of Gray-Level Glass Mask

The generation of gray-level glass mask pattern is performed by using a focused laser beam of 640 nm wavelength to write on a pre-darkened silver ion-exchanged high-energy-beam sensitive (HEBS) glass. The original silver ion-exchanged layer is transparent at visible wavelength. The composition of the HEBS glass makes the ion-exchanged layer insensitive to exposure at visible and near UV wavelength. Only high-energy beam such as accelerated electron beam can darken the ion-exchanged layer by converting silver ions to silver particles<sup>[33-35]</sup>. It is believed that the conduction energy level of the AgX-containing microcrystals is raised relative to its valence band, and is also raised relative to the valence band of the filled conduction level of the contacting metallic silver particles and/or specks, via the addition of photosensitivity inhibitors in the glass melt. The increased band gap energy and electron trapping for the secondary and tertiary electrons make the ion-exchanged glass only sensitive to high-energy-beams such as accelerated electron beams. Therefore, the silver ion-exchanged HEBS glass exhibits different light sensitivity properties as conventional photographic emulsions and photosensitive colored glasses.

The darkened ion-exchange layer with thickness of 3  $\mu\text{m}$  is strongly absorbing to visible laser light showing optical density of about 3.4 at 640 nm wavelength. Heating can result in ionization, converting the silver particles and/or specks to silver ions, thus changing the darkened layer back to transparent one. The heat effect bleaching temperature is determined to be above 140 °C that is substantially below the softening point of the ion-exchanged layer and below the strain point of the glass body.

Focused laser beam writing with red laser wavelength can result in local heating and ionization, thus changing the local darkened layer back to transparent one. Optical mask patterns with excellent contrast can, therefore, be achieved in the ion-exchanged glass layer. By controlling the amount of silver particle ionization through laser writing parameters, gray-level mask patterns can be generated.

The relationship between the laser written transmittance and the laser writing power is given in Fig. 2-14. For the writing calibration the laser writing speed was set at 444  $\mu\text{m/s}$  while the focused laser spot size was 0.8  $\mu\text{m}$ . Excellent control of the written pattern transmittance has been achieved with writing error less than 3%.

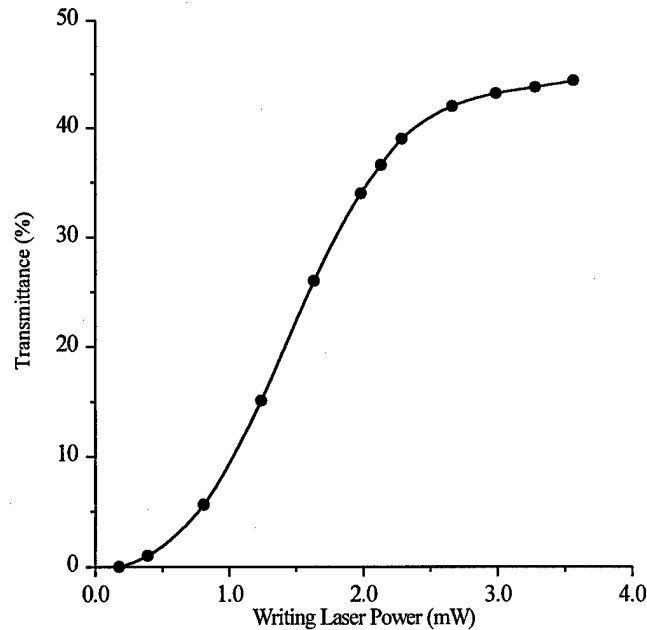


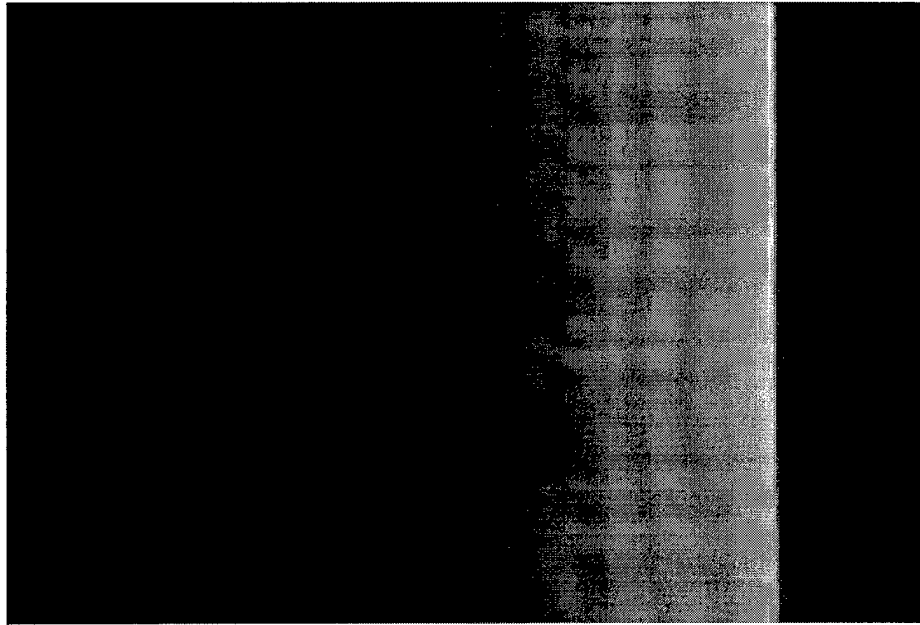
Figure 2-14

Relationship between laser written transmittance and the writing laser power demonstrated by us in an earlier experiment <sup>[33]</sup>.

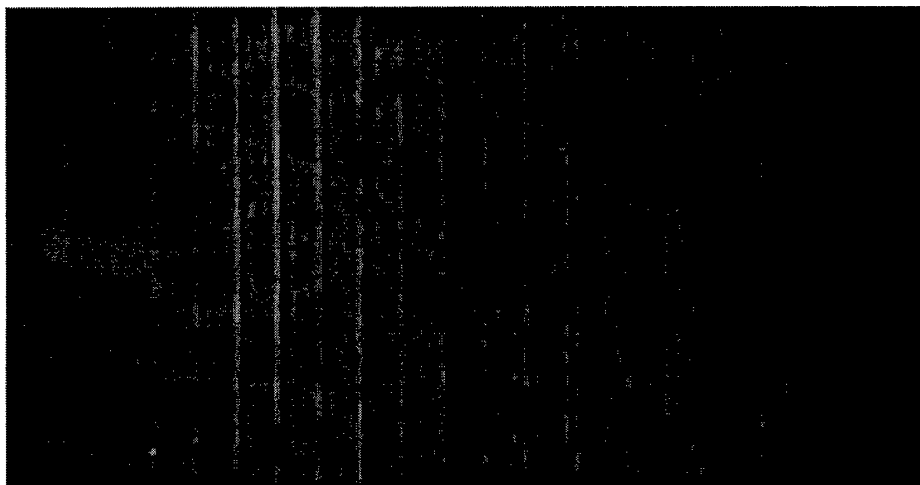
## 2.5.2 Direct Chemical Etching of Surface Relief Structure

The HEBS glass surface can be etched by a common glass corrosive, such as diluted hydrofluoric acid. Transmittance dependent different etching rate has been observed on the ion-exchanged glass layer <sup>[33]</sup>. The etching depth is found to depend on the gray-transmittance of the laser written portion, concentration of the diluted hydrofluoric acid, etching time, and environmental temperature. With proper etching calibration, a single-step wet chemical etching in a diluted hydrofluoric acid is expected to yield precise multi-phase-level surface relief structures.

To quantify the relationship between the relative etching depth and the laser written transmittance distribution, we have first laser written 16 gray transmittance steps as shown in Fig. 2-15(a). Figure 2-16(b) is the microphotograph of the sample etched by 3.3 % diluted hydrofluoric acid for 29 minutes under the environmental temperature of 20 °C. Surface relief profiles were obtained. The etched surface relief structures were evaluated by a TENCOR Alpha-Step 100 surface profiler.



(a)



(b)

Figure 2-15

Picture of the gray-level pattern (a) and its etched surface (b) for calibration purpose.

The etching depth is a relative value that compares measured depth to the surface associated to the laser non-written region. Figure 2-16 shows the etching calibration curve with horizontal axis as original glass transmittance while the vertical axis as the etched depth. By combining the calibration curve of Fig. 2-14 and the curve of Fig. 2-16, we obtain the direct relationship between the laser writing power and the etched depth as shown in Fig. 2-17 that was obtained at laser spot size of  $1\text{ }\mu\text{m}$  and  $444\text{ }\mu\text{m/s}$  writing speed. Here, laser spot size, writing speed, hydrofluoric acid concentration, environmental temperature, and etching time are all fixed.

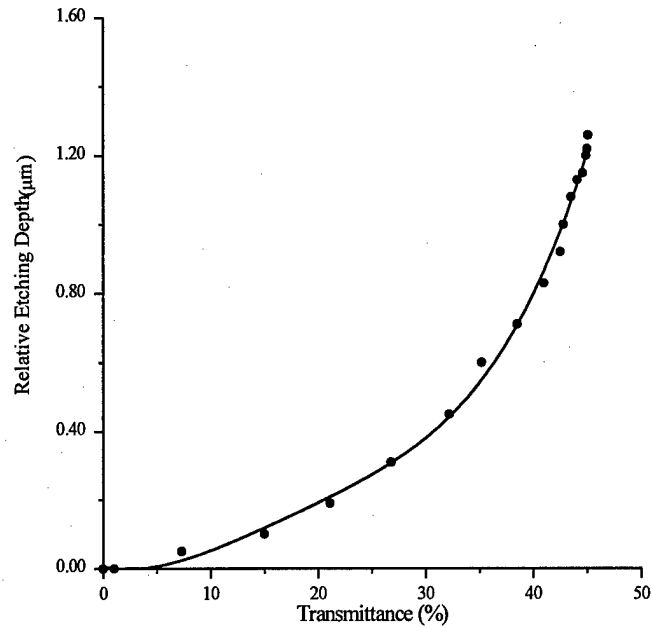


Figure 2-16

Etching calibration showing the relationship between the etched depth and the original transmittance measured at 640 nm wavelength.

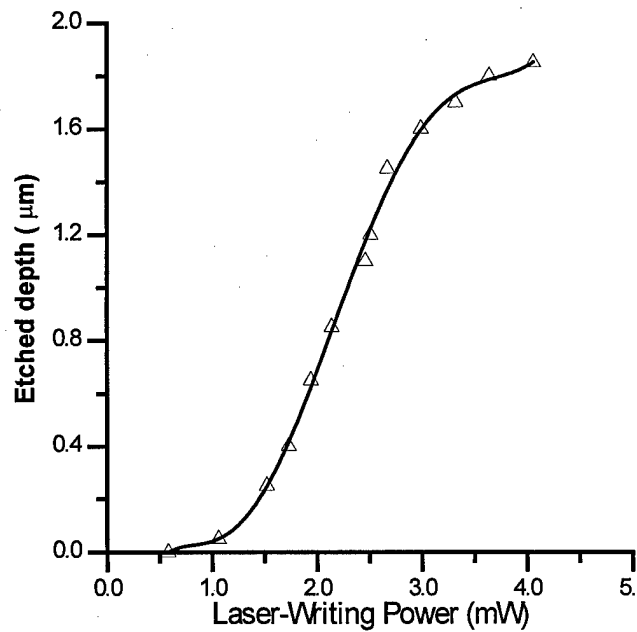


Figure 2-17

Calibration curve of etched depth vs. laser writing power. Laser wavelength, spot size, writing speed, are 640 nm, 1 μm, and 444 μm/s, respectively. Etching is performed in 3.3% diluted hydrofluoric acid at 20°C for 30 min.

### 2.5.3 Realization of Beam Shaping Element

Based on the known refractive index of the HEBS glass that is 1.55 at 633 nm wavelength, we determined that 1.15  $\mu\text{m}$  etched depth corresponds to a  $2\pi$  phase change at the wavelength of 633 nm. Thus, we can directly translate the calculated phase profile of Fig. 2-6(b) to the laser power requirement at each coordinate position. (We note here that in Phase I we use HeNe laser at 633 nm wavelength to demonstrate the feasibility of the proposed concept. In Phase II, we will use near infrared vertical cavity surface emitting laser array.) Figure 2-18 shows the transmissive micrograph of the gray-level pattern of the beam shaper, taken from a microscope with 80x magnification power and using a digital camera. After the one-step surface etching in a 3.3% diluted hydrofluoric acid for 30 minutes at room temperature, the ion-exchanged layer was totally etched out and the required relief structure is realized on the transparent HEBS glass. The reflective micrograph of the resulting surface-relief structure is shown in Fig. 2-19. The etched surface was evaluated by TENCOR Alfa-Step 100 profiler and the scanned surface profile, converting to phase, in the unit of  $\pi$  is given in Fig. 2-20. The measured phase profile in solid curve is compared with the calculation result (dashed curve). For the most region the error is within  $0.1 \pi$ . In general, the experimental result is in very close to the theoretical design value.

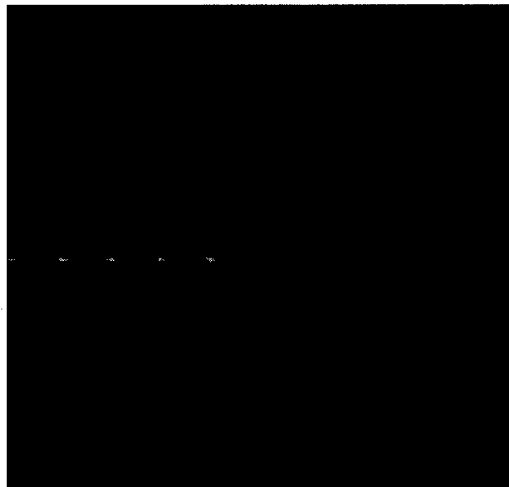


Fig. 2-18

Transmissive micrograph of the laser generated gray-level filter pattern prior to etching.

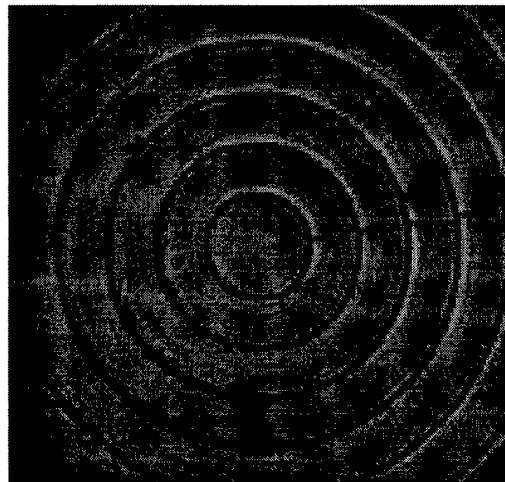


Figure 2-19

Reflective micrograph of the beam shaper after the one-step chemical etching.

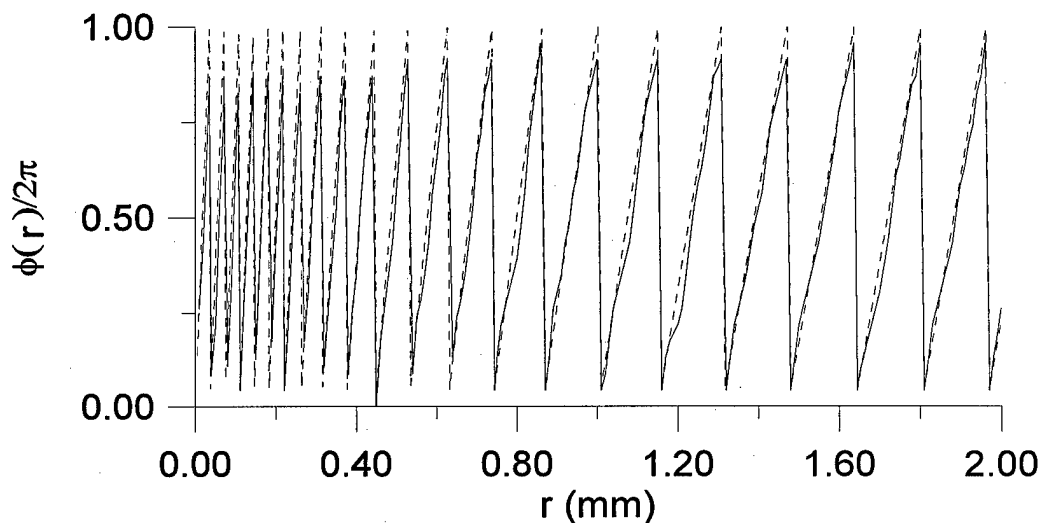


Figure 2-20

Comparison of experimentally realized phase pattern (solid curve) with the theoretical calculation pattern (dashed curve).

## 2.6 Non-Diffracting Beam Evaluation

The performance of the non-diffracting beam shaping filter was evaluated using a CCD camera based optical beam profiler. The schematic of the evaluation setup is shown in Fig. 2-21. The He-Ne laser produced a Gaussian beam at the wavelength of 633 nm. It was expanded by lens system to become a collimated beam with the diameter of 4 mm. The collimated Gaussian beam is incident normally on the filter. The two-dimensional CCD camera was placed after the filter and the captured intensity profile of the shaped beam was evaluated by the window based laser beam profiler software.



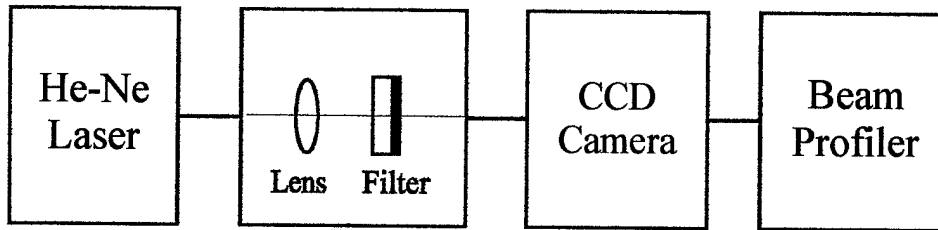
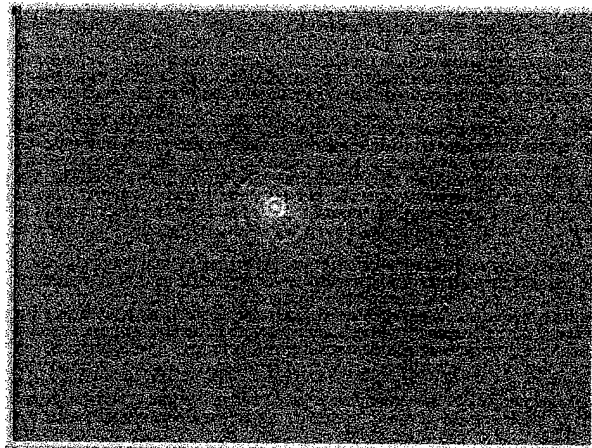


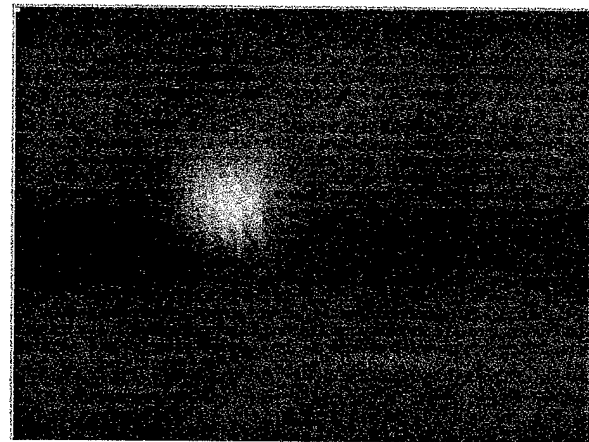
Figure 2-21

Schematic of experimental arrangement for evaluating the performance of the filter.

Figure 2-22(a) is the intensity photograph of the nondiffracting beam profile captured by the CCD camera at a distance of 30 cm from the filter. Figure 2-22(b) is the corresponding photograph of Gaussian beam without the filter. We can see that the central spot of the nondiffracting beam is much smaller than Gaussian beam.



(a)



(b)

Figure 2-22

- (a) The intensity photograph of nondiffracting beam profile at a distance of 30cm from the filter.
- (b) The corresponding photograph of Gaussian beam without the filter.

Figure 2-23(a), (b), and (c) are detailed intensity distribution of the nondiffracting beam profile at different distances from the filter. We can see that the central spot diameter of the nondiffracting beam is 130  $\mu\text{m}$ , keeps almost the same for the three positions.

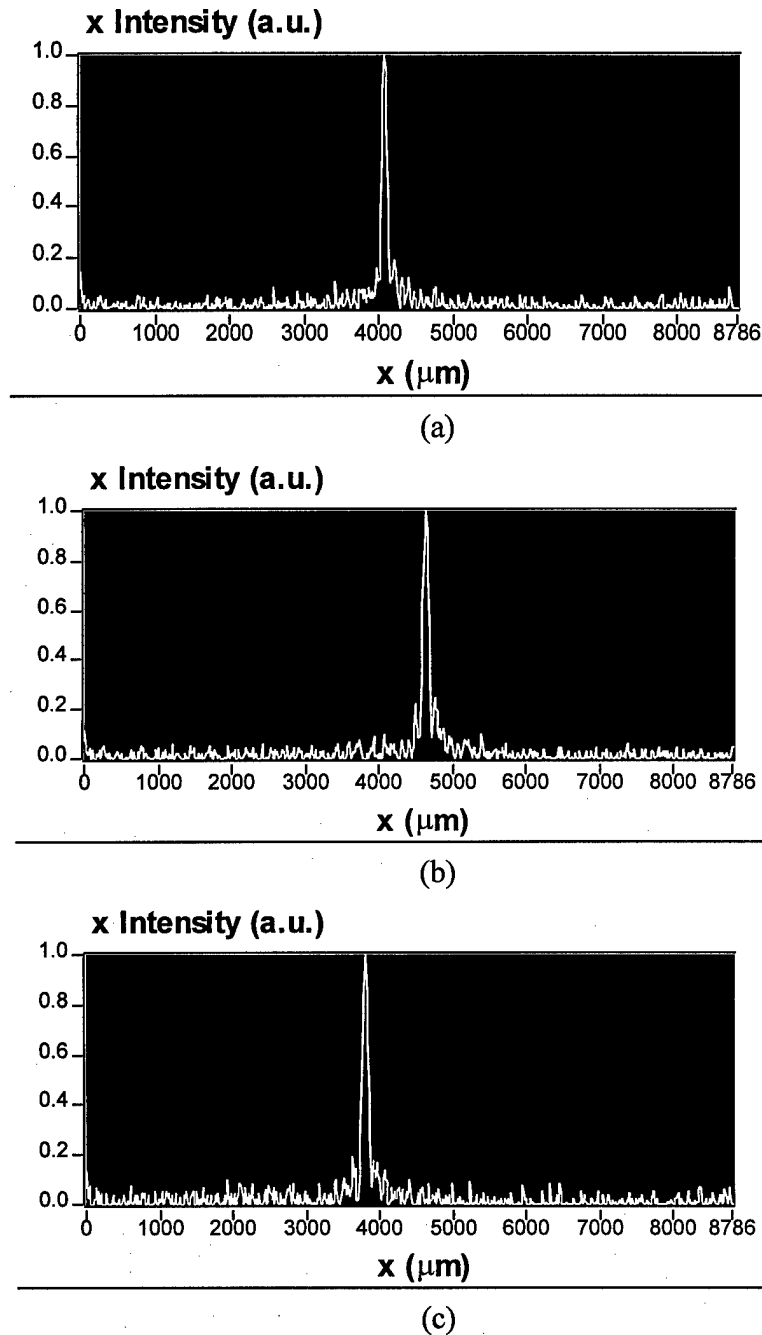


Figure 2-23

Detailed intensity distribution of the non-diffracting beam profile measured at different distances from the beam shaping filter: (a) 20 cm, (b) 30 cm, (c) 40 cm.  $x$  is the transverse coordinate position across the beam center.

Figure 2-24 shows the measured peak intensity distribution in the propagation direction. The experimental result agrees well with the theory. The slight lowering in intensity peak is believed to be caused by the slightly smaller incident Gaussian beam size than the design value. This behavior agrees with the beam size effect explanation given in Sec. 2.4 and Fig. 2-11(a). The measured beam forming efficiency is about 87.5% including the reflection loss from the sample

surface. If we use antireflection coating on the sample surface, the non-diffracting beam forming efficiency can be as high as 92.5%. This is highest non-diffracting beam forming efficiency reported in the literature.

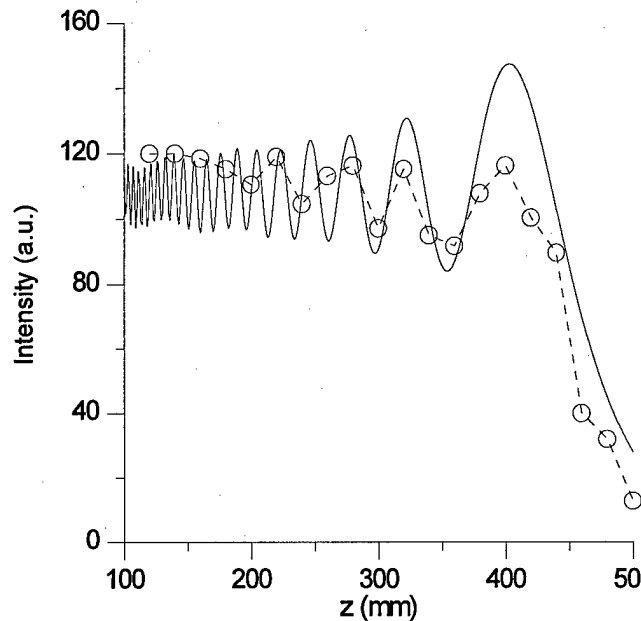


Figure 2-24

Measured intensity distribution with data points in the propagation direction. The calculation curve is also shown for comparison.

## 2.7 Concept of Non-Diffracting Beam Array Formation

The demonstrated non-diffracting beam formed by our DOE beam shaping technique can maintain its pseudo-Bessel beam intensity distribution over the required 40 cm propagation range. It also has a relatively flat peak intensity distribution within such range. The central spot size is about 100  $\mu\text{m}$  (full width measured at  $e^{-2}$  of the peak intensity) while the total beam size including 22 side lobes occupies an area of 2 mm in radius. To form high-density non-diffracting beam array with 250  $\mu\text{m}$  beam center-to-center spacing, there is obvious some overlapping of two neighboring beams as shown in Fig. 1-2. Unavoidably, there will be overlapping in neighboring beam shaper element as shown in Fig.2-25. Such overlapping beam shaper can not be simply produced by diffractive optical element technique. This is probably the drawback of diffractive optics or computer generated holograms, that do not support good spatial, angular, or wavelength multiplexing in the same area.

A volume hologram on the other hand can support spatial, angular, and wavelength multiplexing with excellent reconstruction selectivity. Different reconstruction beam (different incident angle, different incident wavefront, and different incident wavelength) can yield different reconstructed beam output. Such diffraction reconstruction behavior is due to its Bragg diffraction condition rather than a pure phase pattern of computer generated holograms. Thus, using volume hologram technique we can superimpose different non-diffracting beam forming holograms for the construction of high-density non-diffracting beam array. The concept is illustrated in Fig.2-26.

Because a reconstructed non-diffracting beam results only when the Bragg condition is satisfied to its incident beam, it is possible to read one specific hologram with negligible contributions from others.

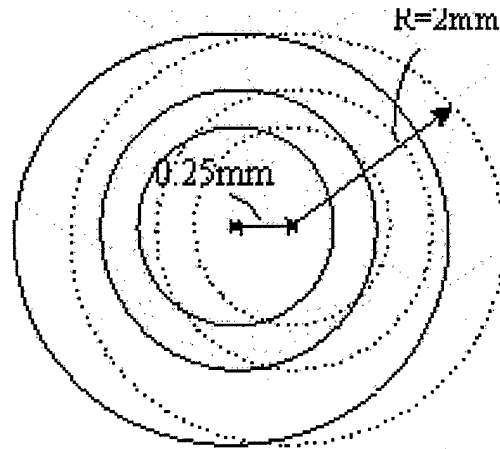


Figure 2-25

Schematic showing the overlapping of pseudo-Bessel beam shaping elements.

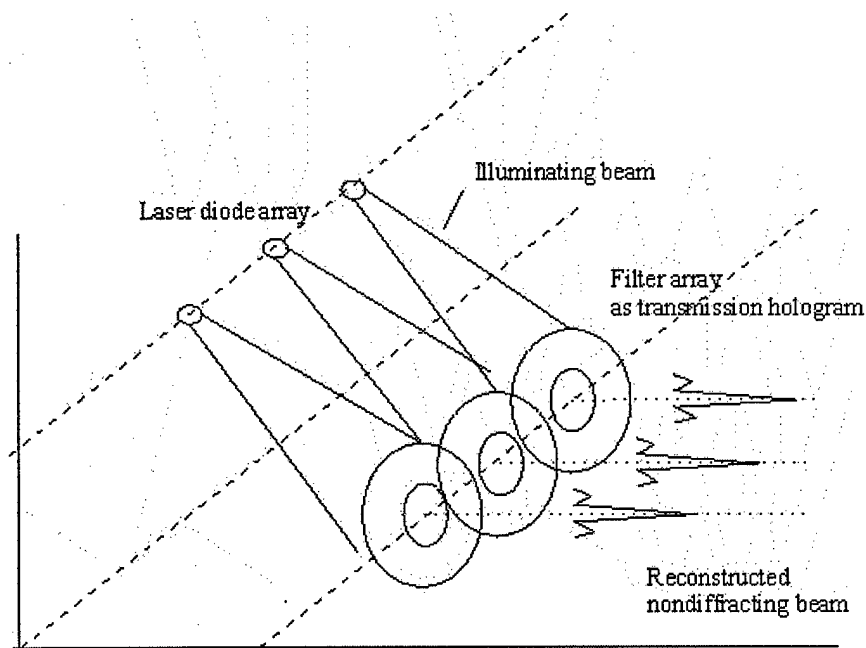


Figure 2-26

Scheme of array non-diffracting beam formation using a superimposed hologram.

Fig. 2-27 shows the schematic of holographic recording setup for the array non-diffracting beam forming. A diode laser beam is a diverging beam. We use here a single-mode fiber to form a diverging beam output that can be used for hologram recording and also used for reconstruction. The HeNe red laser beam (633 nm wavelength) is split into two beams by a beam splitter. One goes through the filter and is transformed into a non-diffracting beam, which serves as the object beam for the hologram. The other beam is focused into a single-mode fiber to form a diverging

output beam, which serves as a reference beam. At the two-beam overlapping region a hologram can be recorded on a holographic recording material. By shifting the position of the holographic recording plate by  $250\text{ }\mu\text{m}$  in lateral direction perpendicular to the two-beam forming plane, we can record a number of such holograms with their spatial overlapping illustrated in Fig.2-26 above. After hologram processing, the reconstruction can be performed by using the same reference beam as the reconstruction beam with the object beam blocked. In this case we should be able to reconstruct the non-diffracting beam one by one by shifting the hologram plate. Successful non-diffracting beam reconstruction should happen when the reconstruction geometry matches with the original recording geometry.

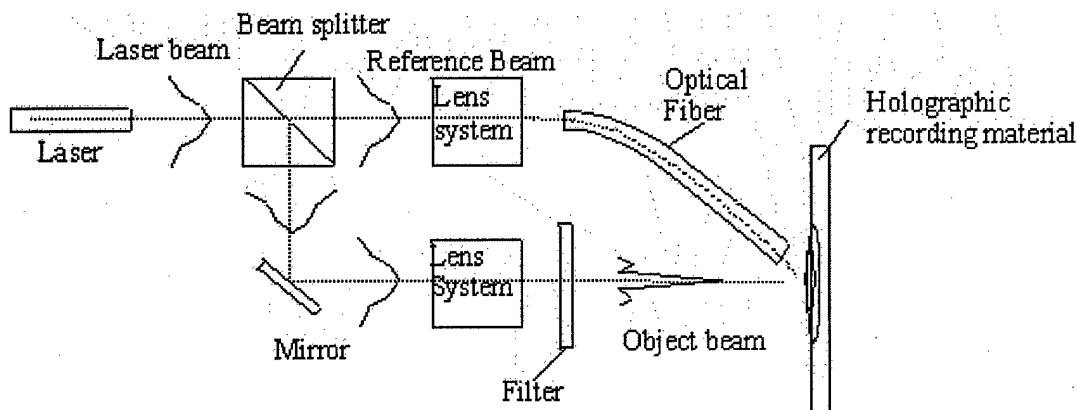


Figure 2-27

Scheme of experimental arrangement for making holographic array beam forming element.

Using an array of diverging reconstruction beams with the same  $250\text{ }\mu\text{m}$  beam spatial separation, as illustrated in Fig. 2-26, we should be able to form the non-diffracting beam array with the same beam center-to-center separation. Given an enough hologram thickness for Bragg condition, the array beam forming should demonstrate negligible crosstalk to the neighboring beams.

## 2.8 Holographic Recording for the Realization of Non-Diffracting Beam Array

### 2.8.1 Holographic Recording Material

It is well known that dichromatic gelatin is an excellent material for recording superimposed volume hologram <sup>[36,37]</sup>. It can demonstrate over 90% efficiency with negligible crosstalk from other superimposed holograms. However, dichromatic gelatin is only sensitive to blue-green recording wavelengths. We are interested in using red or near IR diode laser for interconnect application since they are commercially available and cost effective. However, if we record the hologram at blue or green wavelength while reconstruct the hologram at red or near IR diode laser wavelength we will encounter chromatic reconstruction. Such error can be corrected with a chromatic correction element <sup>[38]</sup>, but is not possible during the Phase I research. We will perform such chromatic correction in Phase II.

To avoid the chromatic reconstruction error, we choose red sensitive holographic recording material – SLAVICH PFG-01 plate for Phase I feasibility demonstration purpose. The SLAVICH PFG-01 plate is purchased from 3DEEP Company. The holographic emulsion thickness is about 10 to 12  $\mu\text{m}$  and the recording sensitivity is about 100 to 300  $\mu\text{J}/\text{cm}^2$  at 633 nm wavelength. The resolving power is about 3000 lp/mm. The holographic processing parameters are summarized in Table II.

Table II Hologram processing procedure for SLAVICH PFG-01 plate.

Name and Sequence of Operations	Time	Chemicals
1. Exposure	--	--
2. Development	1 minute.	Developer: KODAK D-19 developer 156.6 g, add water to make 1 L.
3. Stop Bath	1 minute.	Acetic acid 5 mL, add water to make 1 L.
4. Wash	5 minutes.	Water
5. Bleach	15 seconds after the plate become transparent.	Bleacher: Potasium Dicromate 2 g, add water 500ml, add Sulfuric Acid 10 mL, then add water to make 1 L.
6. Wash	5 minutes.	Water
7. Final Rinse	30 seconds.	KODAK E-6 final rinse (Foto-flo).

The hologram reconstruction efficiency depends largely on the recording process and the recording and reconstruction geometry. Since the hologram is only 10 to 12  $\mu\text{m}$  in thickness, it is not thick enough to be considered as a truly volume hologram and thus the diffraction efficiency will be low and the reconstruction may yield multiple reconstruction beams (higher order diffraction effect). Nevertheless, the SLAVICH PFG-01 plate can be used to demonstrate the feasibility of high-density non-diffracting beam array formation concept.

### 2.8.2 Exposure Time and Diffraction Efficiency

As the first step, we used a collimated Gaussian beam with the diameter of 4 mm to be the reference beam, whose power was 1.42 mW. The recording schematic is shown in Fig. 2-28. To achieve proper two-beam intensity combination we used a pair of polarizers to adjust the power of objective beam to be 0.38 mW. The angle between reference beam and objective beam was  $15^\circ$ . The exposure time was controlled by a shutter. After the formation of the hologram, the objective beam was blocked. Only the reference beam was used to reconstruct the non-

diffracting beam in the transmissive reconstruction geometry. We have tried different exposure time. The optimal exposure time was 1/60 second at the above fixed processing parameters. The reconstruction efficiency was measured to be 16.9%. The low reconstruction efficiency is believed to be due to the present holographic plate limitation as mentioned. The laser recording power density was  $239 \mu\text{J}/\text{cm}^2$ , which agreed well with the recording material parameters.

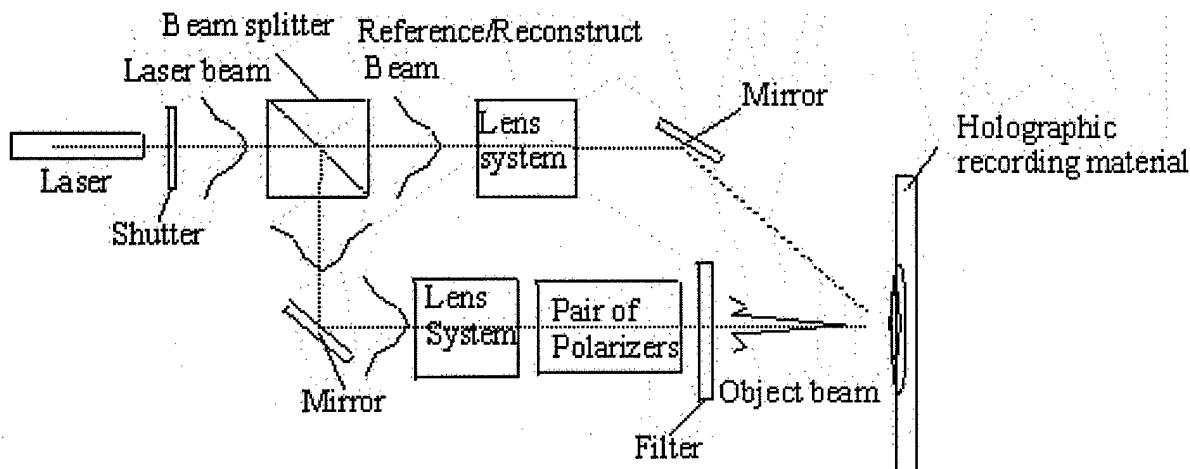


Figure 2-28

Experimental setup for the recording of beam forming hologram using a collimated Gaussian reference beam.

Reconstruction directly from a diverging diode laser beam is of interest since it eliminates any collimation optics. The schematic of using diverging beam for hologram recording is given in Fig. 2-27. Figure 2-29 Shows a photograph of such experimental setup. We used a single-mode optical fiber to simulate the diverging beam from a diode laser. As mentioned before the collimated Gaussian beam was coupled into the optical fiber by a lens system. The expanding output beam of the optical fiber was used as a reference beam for recording. The reference beam diverging angle was about  $20^\circ$ . The distance between the end of fiber and the holographic plate was 1 cm. The power of reference beam was  $1400 \mu\text{W}$ , while the power of object beam was adjusted to  $350 \mu\text{W}$ . The angle between reference beam and object beam was  $15^\circ$ . Again the same hologram processing procedure and parameters shown in Table II was used to develop and fix the hologram. To reconstruct the non-diffracting beam, the recorded holographic plate was placed in the same location for recording. This time the diverging reference beam was used as reconstruction beam while the object beam was blocked. The non-diffracting beam was successfully reconstructed with a measured beam forming efficiency of 12.3%. The corresponding optimized exposure time was determined to be 1/250 second. Details on non-diffracting beam forming quality had been evaluated and summarized below.

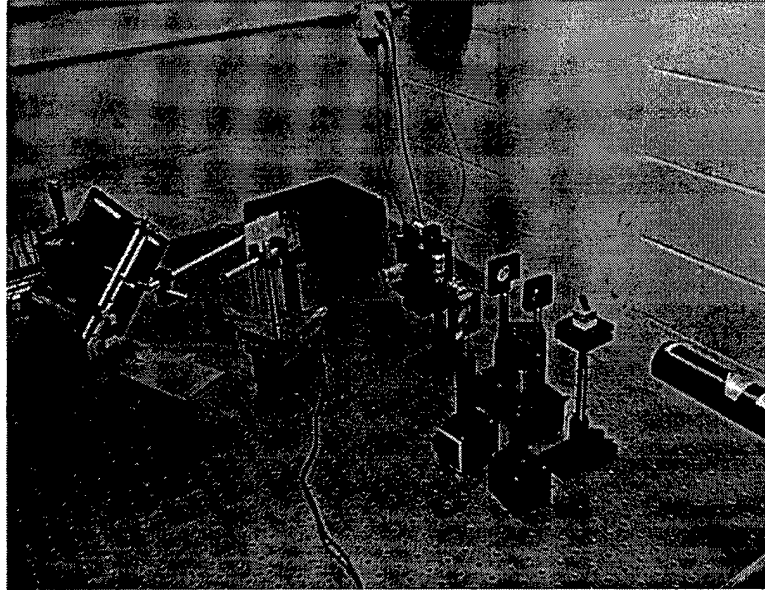


Figure 2-29

Experimental setup for the recording of beam forming hologram using a diverging Gaussian reference beam from a single-mode fiber.

### 2.8.3 Evaluation of the Reconstructed Non-Diffracting Beam

We evaluated the output reconstructed beam from the hologram by a laser beam profiler. Figure 2-30 shows the intensity photograph of the reconstructed beam profile at the distance of 30 cm from the hologram plate. Fig. 2-31(a), (b), and (c) show detailed intensity distribution of the reconstructed beam at different distances from the hologram plate. We can see that the central spot diameter of the reconstructed beam was again 130  $\mu\text{m}$  (peak to zero diameter) or 100  $\mu\text{m}$  (full width at  $e^{-2}$  of the peak intensity), the same as the objective non-diffracting beam used for recording. The central beam spot size was kept almost unchanged for the three positions. This demonstrated that the reconstructed beam has the expected non-diffracting property. This also demonstrated that a single hologram can be effectively used to transform a incident diverging Gaussian beam into a truncated non-diffracting beam. To our knowledge, this is the first experiment using a single transmission hologram (a real hologram, not a computer-generated hologram) to generate non-diffracting beam from a diverging wavefront.



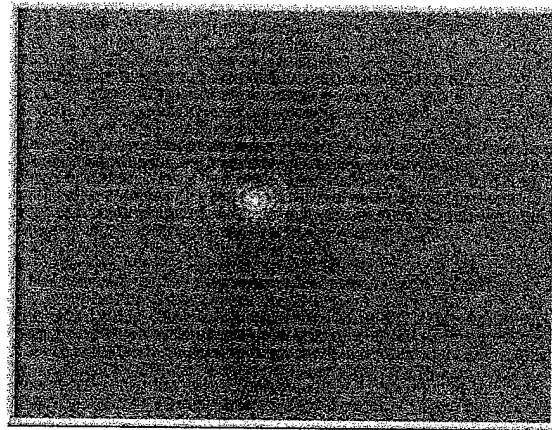
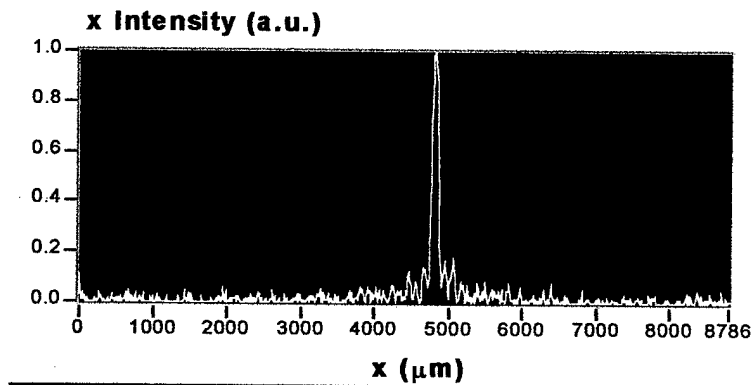
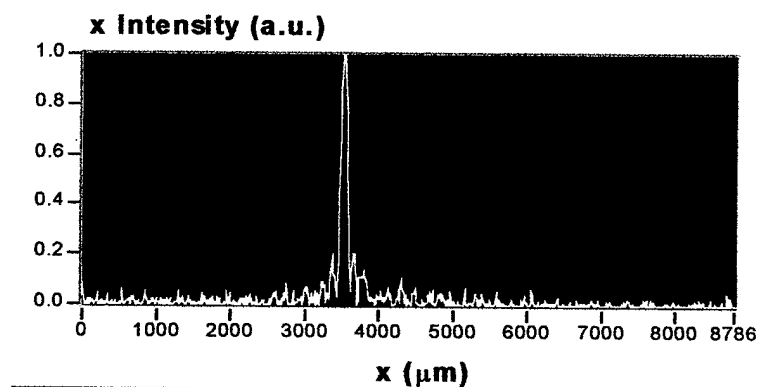


Figure 2-30  
Intensity photograph of reconstructed beam profile at a distance of 30cm from the hologram plate.



(a)



(b)

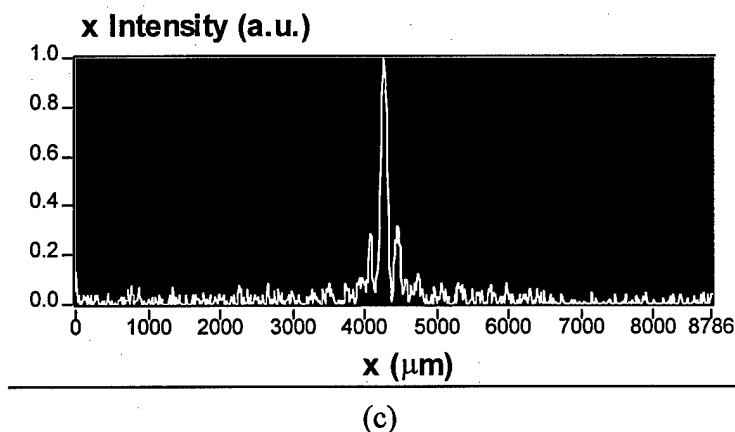


Figure 2-31

Detailed intensity distribution of reconstructed beam profile at different distances from the hologram: (a) 25cm, (b) 30cm, (c) 35cm. X is the transverse coordinate position across the beam center.

## 2.9 Demonstration of High-Density Non-Diffracting Beam Array

One of the key advantages of using the non-diffracting beam is its capability of forming high-density non-diffracting beam array for optical interconnect applications. The concept of forming high-density non-diffracting beam array is illustrated in Fig. 1-2 and in Sec. 2.7. To realize such non-diffracting beam array from an array of diverging beams we need to record superimposed holograms using the recording schematic of Fig. 2-27 and shifting the recording center after each hologram recording. In our design, we consider 250  $\mu\text{m}$  spatial shift that can realize center-to-center non-diffracting beam separation of 250  $\mu\text{m}$  identical to that of standard fiber ribbon. The difference is that the beam is now in free space with enough propagation length without significant beam divergent rather than in a fiber ribbon. The advantage of this approach as mentioned in Sec. 1.0 is to gain simultaneously the advantages of free space interconnection and high-density interconnection that would otherwise be impossible by using conventional Gaussian beam technique.

After recording and developing of two superimposed holograms, we put the holographic plate back, blocked the object beam, and used the reference beam as reconstruct beam to form the reconstructed non-diffracting beam. Again we evaluated the output reconstructed beam from the hologram by the beam profiler. Fig. 2-32 (a) shows the intensity distribution of the reconstructed non-diffracting beam at the distance of 30 cm from the holographic plate. Then the holographic plate was moved 250  $\mu\text{m}$  transversely so that the other superimposed hologram was illuminated by the reconstruct beam with the correct incident condition. The corresponding intensity distribution of the output beam is shown in Fig. 2-32 (b). From both Fig. 2-32 (a) and (b) we can see that the central spot diameter of the reconstructed beams is 130  $\mu\text{m}$  close to the design value. We observed similar beam size at other propagation location within the range. Though there were overlaps between the two holograms, the shape of the reconstructed beams were almost the same as the reconstructed beam from the single hologram. This proved that the reconstructed beam from the superimposed hologram is a non-diffracting beam (pseudo Bessel beam). In either of Fig. 2-32 (a) and Fig. 2-32 (b), the intensity on the transverse position of 250  $\mu\text{m}$  from the

beam center is less than 10% of the intensity of the beam center in the other figure, which means that the maximum crosstalk level is less than -10dB.

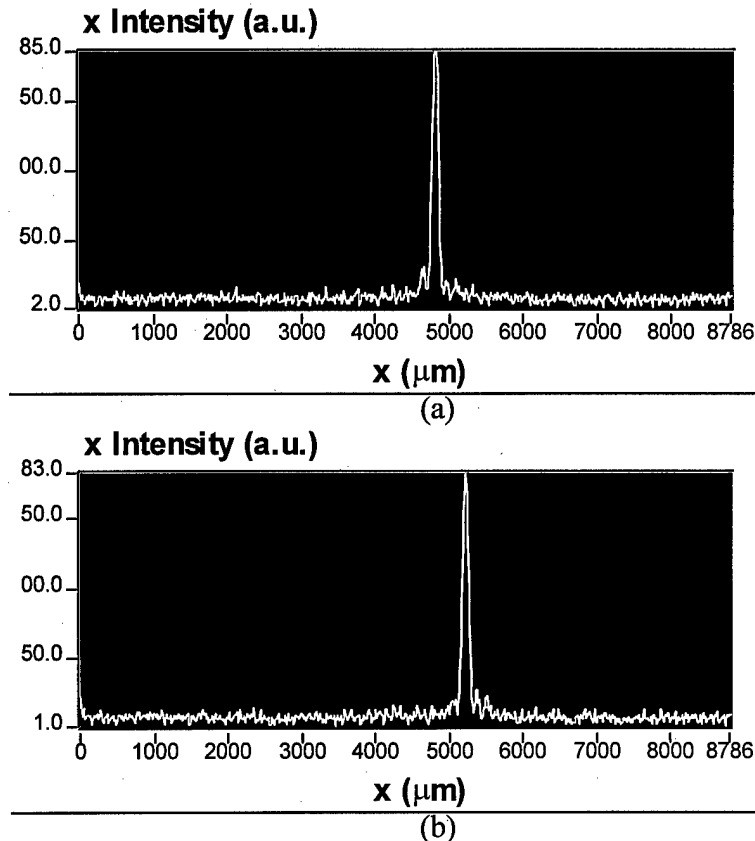


Figure 2-32

Intensity distribution of reconstructed beam profile at a distance of 30 cm from the holographic plate: (a) Reconstruct beam illuminated and aligned with the left hologram. (b) Reconstruct beam illuminated and aligned with the right hologram. Here X is the transverse coordinate across the centers of the two beam shapers.

By keeping the holographic plate unmoved while moving the fiber and the incident diverging beam position in the transverse direction but parallel to the hologram array direction, we reconstructed the non-diffracting beam from each separate hologram after every movement of 250 μm. Each reconstruction we formed a non-diffracting beam parallel to the previous one with 250 μm separation. Figure 2-33 shows the picture of non-diffracting beam array taken by multiple exposure with a fixed camera position located at 30 cm from the hologram. This demonstrated the feasibility of forming high-density non-diffracting beam for optical interconnect applications.

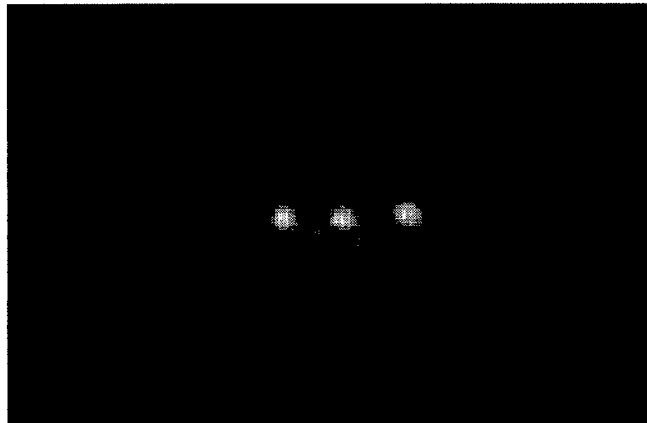


Figure 2-33

Picture of the non-diffracting beam array with 250  $\mu\text{m}$  spatial separation of neighboring beams.

Besides the non-diffracting beam array shown in Fig. 2-33, there is also non-aligned reconstruction. For example, when a diverging laser beam is aligned with one hologram for correct reconstruction, this same beam can also result in undesirable reconstruction by the other superimposed holograms in the same area at non-Bragg condition. Because the directions of the non-Bragg reconstructed beams are not in the desired propagation direction, these beams will not affect the optical interconnect beams. The angle between the non-Bragg reconstructed beam and the Bragg reconstructed beam is about  $15^\circ$  in our case. So the undesired reconstructed beam was beyond 2.5 mm away from the center of the desired reconstructed beam after propagating 10 cm from the holographic plate. These unwanted beam will not affect the array optical interconnect performance but will lower the beam forming efficiency. These unwanted beams can be eliminated by using thicker holograms that will increase the angular selectivity of each hologram.

The crosstalk between adjacent interconnect channel is a critical parameter. Because of the overlapping of the non-diffracting beam peak with the neighboring beam side lobes, there is some signal crosstalk. Our experimental measurement indicated that the crosstalk level is about -10 dB of the central peak signal level. The proposed high-density interconnect concept is thus suitable for digital signal board-to-board interconnection.

## 2.10 Demonstration of Central Lobe Reformation

The non-diffracting has a unique feature of reforming the central lobe when the central lobe is removed. The removal of central lobe can typically happen when placing a photodetector of the size of the central lobe at the central lobe location and use transparent electrode to allow all side lobes to be transmitted. This is known as Bessel beam shadowing and has been demonstrated by MacDonald et al <sup>[24]</sup>. In this Phase I, we also confirmed such behavior. We demonstrated that the removed central lobe can be reformed after 20 mm of propagation from the photodetector.

The Bessel beam shadowing can be used, as shown in Fig. 2-34, to construct high density cascaded board-to-board broadcasting interconnection with signal sending to many interconnect boards at the same time. For example, for a five-board system shown in Fig. 1-4, the optical

signal can be sent from board 1 to boards 2 to 5. To avoid disturbing the side lobes, the density of the photodetectors on boards 2 to 4 should be relatively low not to occupy all the available photodetector positions. This will allow more side lobes to penetrate for central lobe reformation. For example, if we form 1600 high-density interconnect array beams in  $1 \text{ cm}^2$  area, we may allow up to 200 photodetectors in the transmitting area on each board 2 to 4 to receive some of the array signals and keep the array interconnect beams unaffected by the Bessel beam shadowing concept. On the last board 5, we may use all 1600 photodetectors as we wish to receive all the interconnect signals.

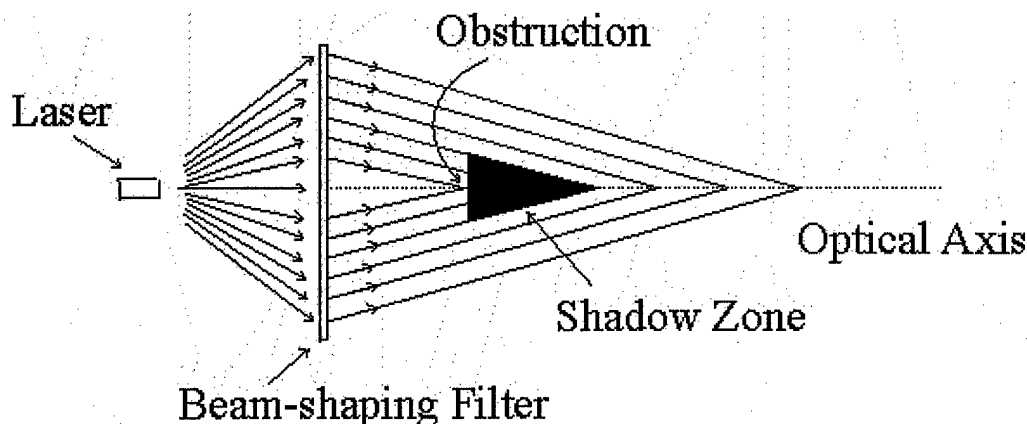


Figure 2-34

Use of Bessel beam shadowing concept for high-density board-to-board optical interconnection.

## 2.11 Discussion on Efficiency and Related Issues

The demonstrated high-density non-diffracting beam array formed by using a SLAVICH PFG-01 type holographic plate has low efficiency due in part to the limitation of the holographic material and in part to the limited holographic emulsion thickness. In a prior experiment demonstrated by Prof. Michael Wang on constructing superimposed holograms for WDM devices using dichromated gelatin as hologram recording media, the diffracting efficiency for each beam was range from 47% to 72% with average of 61% <sup>[36]</sup>. In another experiment demonstrated for 1 to 30 fanout also using superimposed hologram technique (superimposing 30 holograms in the same area), the achieved overall efficiency was 87.8% <sup>[37]</sup>. Obviously, dichromated gelatin can offer much higher reconstruction efficiency than the SLAVICH PFG-01 holographic plate. The dichromated gelatin holographic emulsion can be spin coated with thickness up to  $100 \mu\text{m}$ . It is thus possible to form true Bragg hologram to eliminate higher-order reconstruction and non-aligned beam reconstruction. All these can contribute to the increasing of the overall beam forming efficiency. As discussed in Sec. 2.7, the dichromated gelatin is only sensitive to blue-green wavelength. To form high-density non-diffracting beam array for red or near IR diode laser beam, chromatic correction must be considered. This will be examined in Phase II.

## 2.12 Optical Interconnect Power Budget Estimation

To estimate the optical power budget of the non-diffracting beam interconnect we need to consider several factors including non-diffracting beam forming efficiency, percentage of power

in the central lobe of the non-diffracting beam, and power accepting efficiency at the photodetector. Assume laser power of 1 mW and the holographic beam forming efficiency of 60% (based on the previously demonstrated superimposed hologram efficiency), the non-diffracting beam has the total power of about 0.6 mW. Consider the present situation of non-diffracting beam with 22 side lobes and each side lobe ring contains same about of energy, the central lobe should thus has 26  $\mu$ W of optical power. Such power level is capable of supporting optical interconnect systems with low bit error rate of  $10^{-15}$  requirement<sup>[24]</sup>. Removing one central lobe in cascaded interconnection only affects 4% of total beam energy. It has thus little effect to the power budget for the cascaded interconnect application. The high-density non-diffracting beam array is suitable for board-to-board optical interconnect application.

### **3.0 ADVANTAGES OF THE HIGH-DENSITY NONDIFFRACTING BEAM INTERCONNECTS**

The major advantages and uniqueness of the proposed high-density optical interconnection with free space non-diffracting beams are:

1. Using free-space non-diffracting beams is a new technique for free-space optical interconnection.
2. The free-space non-diffracting beam offers small beam size and little beam broadening over a substantial propagation distance. This is not possible by conventional Gaussian beam.
3. Using free-space non-diffracting beam can achieve high optical interconnect density similar or comparable to guided-wave approach.
4. The free-space interconnection architecture with the non-diffracting beams still preserve the advantages of the free-space interconnects including cross-over interconnects with no crosstalk, ease in interconnect pattern reconfiguration, and low optical propagation and coupling losses.
5. The beam-shaping element for the non-diffracting beam can be a single-element device that minimizes the number of elements involved.
6. Using the non-diffracting beam can increase the depth of focus. It is useful for laser welding, cutting, and medical surgery.
7. Using the non-diffracted beam for board-to-board interconnection can eliminate the needs for collection/focusing lens on the receiving end. Since the non-diffracting beam is small with center peak diameter less than 100  $\mu$ m, the center peak can be directly aligned to the photodetector's sensitive area that can be about 100  $\mu$ m in diameter for over Gb/s operation bandwidth. In this way the conventional focusing element is eliminated.
8. The non-diffracting beam can be easily achieved by our in-house laser generation of gray-level transmittance and phase patterns.
9. The fabricated beam-shaping element with gray-level transmittance and phase patterns on a special high-energy-beam sensitive glass is very stable. It can survive at temperature up to 140°C and at any humidity condition. Exposure to actinic radiation in typical application environment is not harmful to the device.

10. The non-diffracting beams can be generated in array format at low cost based on our laser direct-write gray-level glass mask technology and holographic technology.
11. The proposed high-density free-space optical interconnects based on the non-diffracting beams will result in near-term commercial development of the elements.
12. The beam shaping elements can also find many other applications detailed below.

#### **4.0 POTENTIAL POST APPLICATIONS**

The non-diffracting beam based high-density optical interconnection can improve the performance and computing capability of compact packaged opto-electronic systems. These opto-electronic packaged systems will definitely benefit military applications. For example, they can be employed in high speed and reliable processors such as in missile interceptors for target recognition and firing control. It can also be used to protect other military electronic systems against EMI related electronic jamming.

The non-diffracting beam shaper is expected to meet military environmental specifications, including humidity, temperature cycling, thermal shock, vibration, etc.

The high-density optical interconnection can also help realizing an optical "pin" grid array without the use of many sophisticated lens elements for a 3-D packaged multi-chip module systems (see Fig. 1-6). It can also benefit high speed computers by replacing conventional electrical data buses by the non-diffracting beam optical data buses with the non-diffracting beams transmitting information in an optical substrate (see Fig. 1-5). For this application, the non-diffracting beam is extremely important since there are no sophisticated on-axis lenses in the transparent substrate medium and the high-density interconnection does not permit to use many lenses. With the help of the non-diffracting beam based high-density optical data bus, the overall computer system speed can catch up with the speed of CPU since optical interconnect is extremely fast.

In addition, using high-density optical interconnection can improve the performance and drop the cost of high-speed electronic instruments such as signal generators, oscilloscopes, detector amplifiers, computers, and transceiver modules. Other potential applications are in data fusion, neural networks, complex multimode radar systems, and high speed general pattern recognition problem solving.

Applying the non-diffracting beam in a larger scale (with range of several kilometers to tens kilometers) can advance the laser radar systems, remove sensing, laser range binding, and laser guided missile interception. When the range is hundreds kilometers the non-diffracting beam can also be used for space to earth optical communication.

High-efficiency non-diffracting beam forming can also find application in laser welding and cutting. It can remove the critical focusing requirement associated to conventional technique. The low cost non-diffracting beam shaper can promote the use of non-diffracting beam for optical alignment required in almost every optical system.

#### **5.0 REFERENCES**

1. J. W. Goodman, F. J. Leonberger, S. Y. Kung, and R. A. Athale, "Optical Interconnections for VLSI Systems," *Proc. IEEE*, 72, 850 (1984)
2. L. D. Hutcheson, P. Haugen, and A. Husain, "Optical Interconnects Replace Hardwire," *IEEE Spectrum*, 24(3), 30 (1987)
3. "New Levels of Hybrid IC Density are Provided by Three-Dimensional Packaging," *Defense Sci.*, 7(5), 65 (1988)
4. M. R. Feldman, S. C. Esener, C. C. Guest, and S. H. Lee, "Comparison between Optical and Electrical Interconnects Based on Power and Speed Considerations," *Appl. Opt.*, 27, 1742 (1988)
5. P. R. Haugen, S. Rychnovsky, A. Husain, and L. D. Hutcheson, "Optical Interconnects for High Speed Computing," *Opt. Eng.*, 25, 1076 (1986)
6. D. H. Hartman, "Digital High Speed Interconnects: A Study of the Optical Alternative," *Opt. Eng.*, 25, 1086 (1986)
7. L. D. Hutcheson, "High Speed Optical Interconnects for Computing Applications," *Proc. SPIE*, 862, 2 (1987)
8. M. R. Feldman and C. C. Guest, "Interconnect Density Capabilities of Computer Generated Holograms for Optical Interconnection of Very Large Scale Integrated Circuits," *Appl. Opt.*, 28, 3134 (1989)
9. A. Guha, J. Bristow, C. Sullivan, and A. Husain, "Optical Interconnections for Massively Parallel Architectures," *Appl. Opt.*, 29, 1077 (1990)
10. B. D. Clymer and J. W. Goodman, "Optical Clock Distribution to Silicon Chips," *Opt. Eng.*, 25, 1103 (1986)
11. D. Z. Tsang, D. L. Smythe, A. Chu, and J. J. Lambert, "A Technology for Optical Interconnections Based on Multichip Integration," *Opt. Eng.*, 25, 1127 (1986)
12. E. E. E. Frietman, W. van Nifterick, L. Dekker, and T. J. M. Jongeling, "Parallel Optical Interconnects: Implementation of Optoelectronics in Multiprocessor Architectures," *Appl. Opt.*, 29, 1161 (1990)
13. K. Matsuda and J. Shibata, "Optical Interconnections and Optical Digital Computing Based on the Photonic Parallel Memory," *IEE Proc. J. Optoelectron.*, 138, 67 (1991)
14. M. R. Feldman and C. C. Guest, "Holograms for Optical Interconnects for Very Large Scale Integrated Circuits Fabricated by Electron-Beam Lithography," *Opt. Eng.*, 28, 915 (1989)
15. L. A. Bergman, W. H. Wu, A. R. Johnston, R. Nixon, S. C. Esener, C. C. Guest, P. Yu, T. J. Drabik, M. Feldman, and S. H. Lee, "Holographic Optical Interconnects for VLSI," *Opt. Eng.*, 25, 1109 (1986)
16. R. K. Kostuk, J. W. Goodman, and L. Hesselink, "Optical Imaging Applied to Microelectronic Chip-to-Chip Interconnections," *Appl. Opt.*, 24, 2851 (1985)
17. M. R. Feldman and C. C. Guest, "Computer Generated Holographic Optical Elements for Optical Interconnection of Very Large Scale Integrated Circuits," *Appl. Opt.*, 26, 4377 (1987)
18. J. Durnin, "Exact Solutions for Nondiffracting Beams. I. The Scalar Theory," *J. Opt. Soc. Am. A*, 4(4), 651-654 (1987)
19. J. Durnin, J. J. Miceli Jr., and J. H. Eberly, "Diffraction-Free Beams," *Physical Review Letters*, 58(15), 1499-1501 (1987)



20. C. Özkul, S. Leroux, N. Anthore, M. K. Amara, and S. Rasset, "Optical Amplification of Diffraction-Free Beams by Photorefractive Two-Wave Mixing and Its Application to Laser Doppler Velocimetry," *Appl. Opt.* 34(24), 5485-5491 (1995)
21. A. J. Cox and D. C. Dibble, "Nondiffracting Beam From a Spatially Filtered Fabry-Perot Resonator," *J. Opt. Soc. Am. A*, 9(2), 282-286 (1992)
22. J. Turunen, A. Vasara, and A. T. Friberg, *Appl. Opt.* 27, 3959 (1988)
23. R. P. MacDonald, J. Chrostowski, S. A. Boothroyd, and B. A. Syrett, *Appl. Opt.* 32, 6470 (1993)
24. R. P. MacDonald, S. A. Boothroyd, T. Okamoto, J. Chrostowski, and B. A. Syrett, "Interboard Optical Data Distribution by Bessel Beam Shadowing," *Opt. Comm.* 122, 169-177 (1996)
25. F. Gori, G. Guattari, "Bessel-Gauss Beams," *Opt. Comm.* 64, 491-495 (1987)
26. J. Rosen, "Synthesis of Nondiffracting Beams in Free Space," *Opt. Lett.* 19(6), 369-371 (1994)
27. J. Rosen and A. Yariv, "Synthesis of An Arbitrary Axial Field Profile By Computer-Generated Holograms," *Opt. Lett.* 19(11), 843-845 (1994)
28. Z. P. Jiang, "Super-Gaussian-Bessel Beam," *Opt. Comm.* 125, 207-210 (1996)
29. R. P. MacDonald, J. Chrostowski, S. A. Boothroyd, and B. A. Syrett, "Holographic Formation of A Diode Laser Nondiffracting Beam," *Appl. Opt.* 32(32), 6470-6474 (1993)
30. N. Davidson, A. A. Friesem, and E. Hasman, "Efficient Formation of Nondiffracting Beams With Uniform Intensity Along the Propagation Direction," *Opt. Comm.* 88, 326-330 (1992)
31. J. Sochacki, A. Kolodziejczyk, Z. Jaroszewicz, and S. Bará, "Nonparaxial Design of Generalized Axicons," *Appl. Opt.* 31(25), 5326-5330 (1992)
32. M. R. Wang and H. Su, "Multilevel Diffractive Microlens Fabrication by One-Step Laser-Assisted Chemical Etching upon High-Energy-Beam Sensitive Glass," *Optics Letters*, 23(11), 876-878 (1998)
33. M. R. Wang and H. Su, "Laser Direct-Write Gray-Level Mask And One-Step Etching For Diffractive Microlens Fabrication," *Appl. Opt.* 37(32), 7568-7576 (1998)
34. X. G. Huang, M. R. Wang, Y. Tsui, C. Wu, "Characterization of Erasable Inorganic Photochromic Media for Optical Disk Data Storage," *J. Appl. Phys.* 83(7), 3795-3799 (1998)
35. C. K. Wu, "High Energy Beam Sensitive Glasses," U.S. Patent, 1994, No. 5,285,517.
36. M. R. Wang, T. Jannson, and G. J. Sonek, "Substrate Wavelength-Demultiplexing Optical Interconnects Based on Superimposed Holographic Gratings and Three-Dimensional Bragg Diffraction," *Opt. Lett.* 18(23), 2068-2070 (1993)
37. M. R. Wang, G. J. Sonek, R.T. Chen, and T. Jannson, "Large Fanout Optical Interconnects Using Thick Holographic Gratings and Substrate Wave Propagation," *Appl. Opt.* 31(2), 236-249 (1992)
38. M. Assenheimer, Y. Amitai, and A. A. Friesem, "Recursive Design for an Effective HOE with Different Recording and Readout Wavelengths," *Appl. Opt.* 27, 4747-4753 (1988)